remote sensing

Article

Photogrammetric Monitoring of Rock Glacier Motion Using High-Resolution Cross-Platform Datasets: Formation Age Estimation and Modern Thinning Rates

Tyler M. Meng [1,*], Roberto Aguilar [1], Michael S. Christoffersen [2], Eric I. Petersen [2], Christopher F. Larsen [2], Joseph S. Levy [3] and John W. Holt [1,4]

[1] Lunar and Planetary Laboratory, University of Arizona, Tucson, AZ 85721, USA
[2] Geophysical Institute, University of Alaska Fairbanks, Fairbanks, AK 99775, USA
[3] Department of Earth and Environmental Geosciences, Colgate University, Hamilton, NY 13346, USA
[4] Department of Geosciences, University of Arizona, Tucson, AZ 85721, USA
* Correspondence: tmeng@arizona.edu

Abstract: The availability of remote sensing imagery at high spatiotemporal resolutions presents the opportunity to monitor the surface motion of rock glaciers, a key constraint for characterizing the dynamics of their evolution. In this paper, we investigate four North American rock glaciers by automatically measuring their horizontal surface displacement using photogrammetric data acquired with crewed and uncrewed aircraft along with orbital spacecraft over monitoring periods of up to eight years. We estimate vertical surface changes on these rock glaciers with photogrammetrically generated digital elevation models (DEM) and digitized topographic maps. Uncertainty analysis shows that the imagery with the highest resolution and most precise positioning have the best performance when used with the automated change detection algorithm. This investigation produces gridded velocity fields over the entire surface area of each study site, from which we estimate the age of rock glacier formation using along-flow velocity integration. Though the age estimates vary, the ice within the modern extent of these landforms began flowing between 3000 and 7000 years before present, postdating the last glacial maximum. Surface elevation change maps indicate present-day thinning at the lower latitude/higher elevation sites in Wyoming, while the higher latitude/lower elevation sites in Alaska exhibit relatively stable surface elevations.

Keywords: photogrammetry; rock glacier; kinematics; UAS; airborne; satellite; flow; ablation; Alaska; Wyoming

Citation: Meng, T.M.; Aguilar, R.; Christoffersen, M.S.; Petersen, E.I.; Larsen, C.F.; Levy, J.S.; Holt, J.W. Photogrammetric Monitoring of Rock Glacier Motion Using High-Resolution Cross-Platform Datasets: Formation Age Estimation and Modern Thinning Rates . *Remote Sens.* **2023**, *15*, 4779. https://doi.org/10.3390/rs15194779

Academic Editor: Giuseppe Casula

Received: 2 July 2023
Revised: 9 September 2023
Accepted: 22 September 2023
Published: 30 September 2023

1. Introduction

1.1. Surface Motion of Rock Glaciers

Mountainous terrains with moderate precipitation and mean annual air temperatures less than or equal to 0 °C often develop ice and lithic-rich landforms known as rock glaciers. The ice units originate under a continuum of surface processes, including the burial of glacial ice by rockfall and ablation lag [1,2], preservation of overlapping debris and snow avalanche deposits [3], and the infiltration/refreezing of liquid water in rocky talus [4,5]. These ice/debris mixtures creep downslope under gravitational driving stresses to form discernible lobate morphologies, often superimposed by ridges, furrows, and flow bands [6]. In general, rock glaciers flow with an average surface displacement on the order of tens of centimeters to meters per year [1,7].

Previous measurements of active rock glacier flow have included both in situ and remote sensing methods. Before the availability of remote sensing data with temporal and spatial resolutions sufficient to track surface movement at the scales of rock glacier creep, surface-based displacement measurements were collected at benchmark positions at various locations along rock glacier surfaces [1,4,8–13]. Early displacement measurements were made by repeatedly calculating the position of surface features in a local coordinate system referenced to stable bedrock points, marking the end of a "movement line". High accuracy and high precision global navigation satellite system (GNSS) positioning has recently allowed for displacement measurements through the monitoring of surface features' absolute positions over known time intervals. These point measurements are only possible at surface locations that are safely accessible and stable for repeated measurement, which limits this form of surface motion data both temporally and spatially.

Recent developments in remote sensing technology have created the opportunity to observe rock glacier flow with higher spatiotemporal resolution. Photogrammetric techniques using data collected via uncrewed aerial systems (UAS), piloted overflights, or optical satellite imagery provide a solution to the spatial limitations of surface-based point measurements of rock glacier surface features, as a photogrammetric orthomosaic encompasses a larger percentage of a rock glacier's surface than a set of ground-based point measurements. In addition to optical imagery, interferometric synthetic aperture radar (InSAR) has been used to measure rock glacier surface displacement with high precision [14–16]; however, such surveys are limited by the orbital geometry of the instrument and the flow direction of each target, as the displacement is measured along the line of sight of the InSAR system. Overall, remote monitoring provides a method to produce regularly repeated measurements of features in rugged and isolated terrain, which benefits time series analysis through the availability of a longer record length and higher sampling frequency. The ability to consistently track rock glacier surface motion has led to significant advances in the understanding of rock glacier kinematics and its relationship with glacier and permafrost dynamics [7,17–24]. New information regarding the extents and magnitudes of rock glacier flow fields addresses Tasks 1, 2, and 3 of the International Permafrost Association Action Group for Rock Glacier Inventories and Kinematics (RGIK) by contributing to a database of rock glacier attributes, including locations, surface areas, and flow velocities [6,25].

With the objective of monitoring rock glacier activity, inferring their flow history, and characterizing their kinematics and dynamics, we present new surface motion measurements on four North American rock glaciers, two in Wyoming and two in Alaska. We use an existing image correlation algorithm to detect feature displacement over time intervals of up to eight years in an analysis using optical imagery collected with UAS, airborne, and satellite platforms. Using the gridded velocity fields of the entire surface area of each rock glacier, we estimate the age of each landform by integrating head-to-toe velocity profiles, then we discuss their relationship with documented glacial advances in the region of each study site. We use the elevation data produced by the photogrammetric processing to estimate surface elevation change and modern rock glacier thinning rates. Our study aims to examine the local heterogeneities in rock glacier evolution by comparing the surface motion and elevation change of two rock glaciers in each geographic region. We achieve these objectives using a combination of UAS, airborne, and satellite imagery with photogrammetric processing and surface change analysis. High-resolution data capturing the three-dimensional change of rock glacier surfaces can provide a foundation for future monitoring campaigns and further investigation of rock glacier dynamics. Our study adds new surface change datasets for four rock glaciers to the existing inventory of rock glacier activity. In addition, it presents novel techniques for evaluating the uncertainty of surface change results and interpreting these results in the context of Quaternary geology.

1.2. Study Areas

1.2.1. Absaroka Mountains, Wyoming

Due to their central location in the contiguous United States and their relative accessibility by road, the small population of rock glaciers in the Absaroka Mountains of northwest Wyoming have been the subject of the longest-lived and most comprehensive studies of any rock glaciers or debris-covered glaciers in North America. Galena Creek Rock Glacier (Figure 1a, henceforth referred to as "Galena Creek") has been the particular focus of heated debate over the origins of ice in rock glaciers. The discussion has centered on whether to classify these features as ice-cored (glaciogenic) or ice-cemented (periglacial) rock glaciers [1,26–28]. Surface boulder displacement monitoring began at Galena Creek in the 1960s [1]. Based on geomorphic and geophysical data, along with observed ice exposures, it was concluded that the upper section of Galena Creek is an active ice-cored rock glacier consisting of glacier ice buried beneath an unconsolidated layer of debris. The debate has continued, as skeptics have attempted to refute the evidence of the glacial ice core [26], although this debate was largely settled in the 1990s when a drilling campaign at Galena Creek retrieved an ice core nearly 10 m long indicating the present-day existence of a debris-covered glacier [29]. This drill core contained a unit of bubbly ice with thin layers of gravel and sand, and the isotopic composition of this ice indicated that it originated as a glacier rather than as frozen interstitial meltwater [30]. Further exploration using ground-penetrating radar (GPR) revealed dipping debris bands in the cirque of Galena Creek, suggesting an ongoing ice accumulation process facilitated by the deposition of debris on the surface of the glacier [3]. On this upper portion of the rock glacier where there is a glacial ice unit, the debris is approximately 0.8–1.5 m thick [31]. With these observations in mind, we interpret the upper two-thirds of Galena Creek to be a debris-covered glacier. In comparison, the lower third of Galena Creek has slower surface velocities, a debris mantle thicker than 2 m, and a lower ice concentration, resembling an older ice-cemented rock glacier modified by periglacial processes and possible interactions with the advancing debris-covered glacier, similar to processes that have been documented at other rock glaciers. [12,31–34].

Sulphur Creek Rock Glacier (Figure 1b, henceforth referred to as “Sulphur Creek”) lies approximately 3 km southeast of Galena Creek. Despite this proximity to Galena Creek, Sulphur Creek has received relatively less geological research attention due to its larger surface area, higher topographic relief, and more difficult access. Historical photos acquired in 1893 during a surveying expedition led by Thomas A. Jaggar, Jr., showed a clean ice glacier in the cirque of the Sulphur Creek basin, with a thin supraglacial debris layer developing a few hundred meters downslope of the location of the terminus of the present-day debris-free snow and ice [35]. Recent GPR measurements indicate a transition from an alpine debris-covered glacieret to a relatively ice-poor rock glacier as elevation decreases along the length of Sulphur Creek [31]. The same measurements showed that the debris on the glacieret ranges from 0.1–1 m thick, while the debris on the lower glacier is greater than 2 m thick. Both Galena Creek and Sulphur Creek follow the Östrem curve [36], showing evidence of sub-debris ice melt where the debris is thin; at the surface of both sites, streams can be heard flowing at the debris–ice interface. These two rock glaciers provide unique examples of the effect of debris supply and valley geometry on ice units transitioning between glaciers, debris-covered glaciers, and rock glaciers [37].

1.2.2. Wrangell Mountains, Alaska

Sourdough Peak is a mountain in Wrangell–St. Elias National Park that hosts two large lobate rock glaciers. The rock glacier flowing down the peak’s southern flank is named Sourdough Rock Glacier (Figure 1d, henceforth referred to as “Sourdough” for simplicity), and the rock glacier flowing down its northwest slope is McCarthy Creek Rock Glacier (Figure 1e, henceforth referred to as “McCarthy Creek”). Sourdough has been surveyed with GPR; these surveys detect a landform thickness of up to 50 m, and the dielectric mixing model indicates volumetric ice concentrations greater than 50 percent based on the radar wave speed within the rock glacier [31]. The ice-free debris thickness measurements at Sourdough are generally greater than 2 m, although runoff can be observed through the sound of localized sub-debris streams despite the thickness of the overburden. The McCarthy Creek site has not been studied with in situ geophysical methods. A surface motion survey at Fireweed Rock Glacier, which is a nearby rock glacier in the Wrangell Mountains, measured velocities exceeding 3.5 $\frac{\text{m}}{\text{yr}}$ [13]. The oversteepened terminus of this rock glacier experiences periodic slope failure events when heavy precipitation swells its proglacial stream, a process that may impact the dynamics of the rock glacier and the characteristics of its velocity field in comparison with Sourdough and McCarthy Creek.

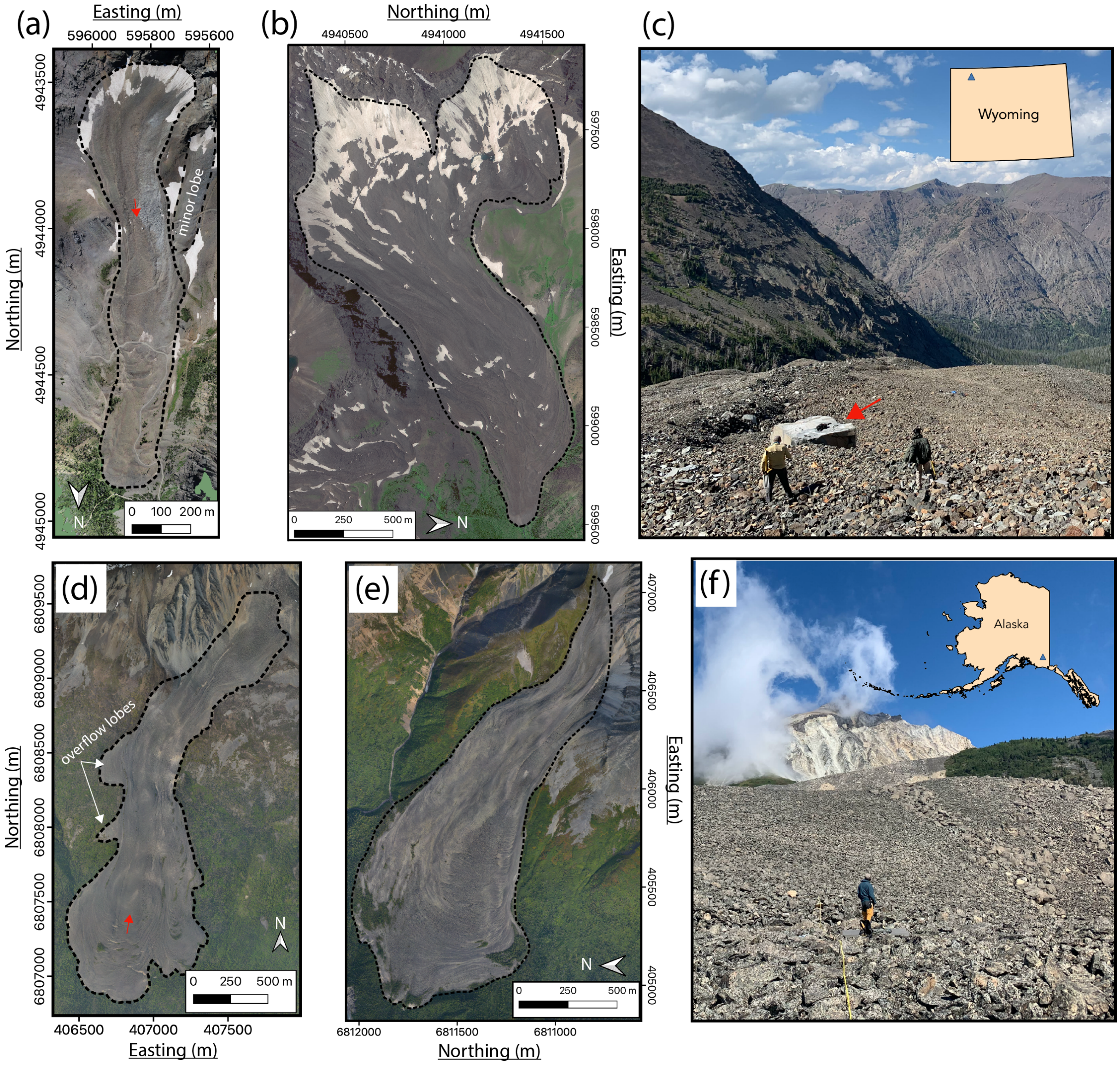

Figure 1. Projected orthomosaics and surface photos showing the rock glaciers targeted in this study. (**a**) Galena Creek Rock Glacier, Wyoming (Galena Creek), UAS image acquired in August 2022 and projected to WGS 84/ UTM Zone 12N. The red arrow shows the location and viewing direction of the photo in panel (**c**). (**b**) Sulphur Creek Rock Glacier, Wyoming (Sulphur Creek), satellite imaged acquired in August 2022 and projected to WGS 84/ UTM Zone 12N. (**c**) Field photo at Galena Creek, showing debris clast size distribution and topographic relief. The red arrow identifies the boulder used for the example in Figure 2. (**d**) Sourdough Rock Glacier, Alaska (Sourdough), airborne image acquired in May 2014 and projected to WGS 84/UTM Zone 7N. The red arrow shows the location and viewing direction of the photo in panel (**f**). (**e**) McCarthy Creek Rock Glacier, Alaska (McCarthy Creek), airborne image acquired in in August 2014 and projected to WGS 84/UTM Zone 7N. (**f**) Field photo at Sourdough. The images have been rotated to make the direction of flow point roughly towards the bottom of the page. All rock glacier outlines presented are the extended delineations [6], including the input talus slopes and front and lateral margins. All subsequent maps use the same projections as those shown here.

2. Materials and Methods

2.1. Photogrammetric Data Acquisition and Processing

For this investigation, our objective was to measure feature displacement with remote imagery over multiple time intervals and compile the longest possible time series of surface displacement for each study site. To detect surface velocities less than 1 $\frac{\text{m}}{\text{yr}}$ at seasonal intervals, it is necessary to use decimeter-resolution imagery to resolve the details of the surface features as well as to detect displacements on the order of decimeters. The imagery for our two Wyoming sites was collected via UAS, crewed aircraft, and satellite platforms between 2020 and 2022. The Alaska sites were targeted by a crewed airborne photogrammetry campaign between 2014 and 2022. Supplementary Figure S1 details the methodological workflow for measuring the surface displacement and elevation change with these combined data sources. Below, we discuss the advantages and disadvantages of these methods at each site and compare our remote sensing results with surface-based boulder displacement measurements at Galena Creek.

2.1.1. Wyoming

In August 2020 and August 2022, we acquired photogrammetry data covering Galena Creek using a DJI Phantom 4 RTK UAS. We used the DJI GS RTK flight planning software in 2D Photogrammetry mode with terrain awareness. In 2022, eight ground control points (GCP) were deployed and surveyed. For both years, the GCP locations were measured using real-time kinematic positioning (RTK) with Emlid Reach RS2 GNSS receivers. The coordinates of the base station were postprocessed with precise point positioning using the Canadian Spatial Reference System Precise Point Positioning tool. We used Emlid Studio software version 1.3 to apply the postprocessing kinematics to the UAS images.

The photogrammetric processing workflow was carried out using Agisoft Metashape Professional software version 1.7.5 build 13229. After the photos were aligned and the dense clouds were created, digital elevation models (DEM) and orthomosaics were generated for further analysis. The detailed parameters used in the workflow for each flight are provided in the processing reports included with the supplementary materials, and the workflow diagram is shown in Supplementary Figure S1. These orthomosaics have a spatial resolution of 7.9 $\frac{\text{cm}}{\text{pixel}}$ for 2020 and 5.4 $\frac{\text{cm}}{\text{pixel}}$ for 2022 (Table 1), and the DEMs have a pixel width double that of their corresponding orthomosaics. In 2022, four points were used as control at Galena Creek, with a root mean square (RMS) error of 0.012 m, and the remaining four points were check point (CP), with an RMS error of 0.068 m. To supplement the two UAS datasets, we purchased satellite imagery from the SkyMap50 system through Soar.Earth, a commercial organization that distributes orbital imagery data. We obtained one complete 41.1 $\frac{\text{cm}}{\text{pixel}}$ SkyMap50 scene of Galena Creek without clouds, acquired on 10 July 2021.

We compared independent motion measurements at Galena Creek using surface-based and remote sensing methods. Large debris clasts on the Galena Creek surface were marked with paint in the 1960s to measure rock glacier surface motion, and the set of marked clasts was expanded and updated with new paint and bolts in the 1990s [1,29]. The paint markings and identifying symbols on the clasts remain legible. We collected positioning data for 22 identifiable marked boulders using the Emlid Reach RTK system in August 2022 and compared these locations to measurements collected in 1997, 1998, 1999, and 2015 [12,29,38]. Because the measurements from the 1990s and 2015 were acquired with a total station, we converted the local coordinate system used for these earlier datasets to the WGS84 / UTM Zone 12N projected coordinate system using a USGS benchmark and stationary points on stable bedrock for direct comparison with the 2022 RTK measurements.

Table 1. List of acquisition details for the imagery used for the change detection analysis at each field site (GC = Galena Creek; SC = Sulphur Creek; SRG = Sourdough; MC = McCarthy Creek). Each date is provided in YYYYMMDD format.

Region	Site	Date	# of Images	Avg. Camera Error (cm)	Resolution ($\frac{\text{cm}}{\text{pixel}}$)	# of GCP/CP	GCP/CP RMSE (cm)
Wyoming	GC	20200823 ^{U}	1076	0.3	7.9	0/0	n/a
	SC	20200825 ^{A}	269	n/a	10.8	10/3	0.44/28.3
	GC	20210710 ^{S}	1	n/a	40.1	0/0	n/a
	SC	20210710 ^{S}	1	n/a	41.0	0/0	n/a
	SC	20220807 ^{S}	1	n/a	41.3	0/0	n/a
	GC	20220808 ^{U}	941	0.8	5.4	4/4	0.97/7.59
Alaska	SRG, MC	20140525 ^{A}	433	16.2	20.0	0/0	n/a
	SRG, MC	20140823 ^{A}	345	17.2	19.8	0/0	n/a
	SRG, MC	20150523 ^{A}	546	15.2	20.6	0/0	n/a
	SRG, MC	20150829 ^{A}	561	18.8	19.3	0/0	n/a
	SRG, MC	20160601 ^{A}	614	14.5	25.3	0/0	n/a
	SRG	20160817 ^{A}	494	21.9	24.2	0/0	n/a
	SRG, MC	20190905 ^{A}	628	65.3	12.1	0/0	n/a
	SRG	20200517 ^{A}	215	9.7	12.4	0/0	n/a
	SRG, MC	20201018 ^{A}	520	80.5	12.4	0/0	n/a
	SRG, MC	20210622 ^{A}	340	11.7	14.8	0/0	n/a
	SRG	20220708 ^{A}	357	26.2	18.5	0/0	n/a

^{U} UAS image; ^{A} Piloted airborne image; ^{S} SkyMap50 satellite image.

At Sulphur Creek, airborne imagery was collected on 25 August 2020 by Kestrel Aerial Services using a Canon EOS 5D Mark III DSLR with a Canon EF 50 mm 1.2 lens. The positioning information was recorded by a Garmin Aera 796 synchronized with the camera clock mounted in the panel of the aircraft. For this acquisition, we used ten GCPs to optimize the positioning of the imagery. The individual images and their positions were delivered as georeferenced TIFF files, and these data were processed in Agisoft Metashape to generate an orthomosaic and DEM. The ten points used as control had an RMS error of 0.0004 m, and three points used as check points had an RMS error of 0.283 m. In addition to the 2020 airborne image, we obtained one partial image and one complete image of a cloudless Sulphur Creek available in the SkyMap50 collection. The image from 7 August 2022, contains the full rock glacier, while the lowest 500 m section of Sulphur Creek is cut off at the eastern edge of the 10 July 2021 scene.

2.1.2. Alaska

The photogrammetry data for Sourdough and McCarthy Creek were acquired during eleven piloted overflights between May 2014 and July 2022 (Table 1). The flights were planned with the objective that more than nine overlapping images would cover the target surfaces. The 2014–2016 images were collected with a Nikon D800 DSLR and the 2019–2022 images were collected with a Nikon D850 DSLR, both with a Zeiss Distagon 25 mm lens. Each raw image was collected in NEF format and postprocessed to maximize contrast before conversion to JPG format. Aircraft positions were measured with a Trimble R7 GNSS receiver recording at 5 Hz. Following [39], an intervalometer was used to trigger event markers in the GNSS data associated with each camera flash. These coordinates were transformed from the GNSS antenna to the camera image plane using a triple coordinate rotation of the measured lever arm for the aircraft's antenna/camera configuration.

By interpolating the camera positions from the 5 Hz GNSS data with the event markers, each image was tagged with a position to approximately 10 cm accuracy [39]. From these tags, a camera position file associating each JPG image name and position was generated and used as a reference for the photogrammetric processing steps. We followed the same Agisoft Metashape workflow described in Section 2.1.1. The individual processing reports for each flight are provided in the supplementary information. Due to logistical limitations in the field, no GCPs were used in the photogrammetric processing for the Alaska sites, and there were no surface boulder measurements or GCPs to provide direct in situ validation for these sites. Sourdough was imaged with all eleven flights, while McCarthy Creek was only imaged on eight of the eleven flights due to variable weather conditions in the narrower McCarthy Creek Valley. The acquisition dates and original resolutions of all rock glacier imagery analyzed in this study are provided in Table 1.

2.2. Change Detection Analysis

To automatically measure the horizontal rock glacier surface displacement between image pairs, we used the free correlation image analysis software CIAS [7,40]. This algorithm, available as a compiled IDL program, requires grayscale images with identical extents and resolutions in a Cartesian coordinate system. We preprocessed the images using the Geospatial Data Abstraction Library (GDAL) within the QGIS user interface. Both of these software packages are open source. To preprocess the images, we used the GDAL *Warp* tool to project the raster data to their appropriate Cartesian coordinate systems from the WGS84 geographic coordinates (UTM zone 7N for the Alaska sites and zone 12N for the Wyoming sites). *Warp* was used to clip the images to an appropriate extent and to resample the images to the resolution of the coarsest image in the pair with the cubic spline resampling method. Finally, the grayscale images used for the change detection input were extracted from the RGB data using the GDAL *Translate* tool.

After preprocessing the images, each image pair in the set was analyzed to derive the surface displacement vectors over the time interval between acquisitions. All of the image pairs at each field site were analyzed using a common set of grid points specified by a file containing the Cartesian coordinates of each grid point. The Galena Creek datasets were analyzed on a 5 m × 5 m grid, while the more extensive Sulphur Creek and Alaskan sites were analyzed on a 10 m × 10 m grid. All of the image pairs were analyzed using normalized cross-correlation and the normal pyramid matching speed. Our experiments with CIAS determined that a reference block of 45 pixels × 45 pixels and a search window of 100 pixels × 100 pixels at each grid point was optimal for correlating surface features and detecting realistic displacements for all of the image resolutions and time periods analyzed (Figure 2). Due to the forest cover surrounding the Alaska sites, which obscured the stable terrain, co-registration was not performed for individual image pairs. Instead, we used the minimum uncertainty in surface displacement as the averaged CIAS-derived displacement value for stable, off-glacier terrain within each scene. We verified these displacement values through manual inspection of stable surface features wherever possible. This added the benefit of decreasing the processing time and avoiding the application of inconsistent uncertainties due to an extra transformation step unique to the processing workflow of each image pair. To convert the displacement results into the surface velocity in $\frac{\mathrm{m}}{\mathrm{yr}}$, we found the precise number of years between images by dividing the number of days between each image pair by 365.25 days per year, then divided the displacement in meters by the time interval in years.

In image pairs for which one or both of the images is a SkyMap50 image targeting Galena Creek or Sulphur Creek, there is a static offset in the images due to limitations in image precision using the positioning of a space-borne camera. To solve this issue of imprecise image co-registration, we first ran the change detection algorithm on the images with their initial positioning information. We selected a subset of displacement vectors over a portion of the images interpreted to be stable bedrock. The mean of this subset of displacement vectors was subtracted from the projected coordinates of the corners of the later image in the image pair to shift the geolocated image using the "-a_ullr" flag in the GDAL *Translate* function to correct for the initial static shift. The largest magnitude of the shifts that were used was 1.56 m for the Galena Creek July 2021 SkyMap50 image; the parameters for each shift are shown in Table 2.

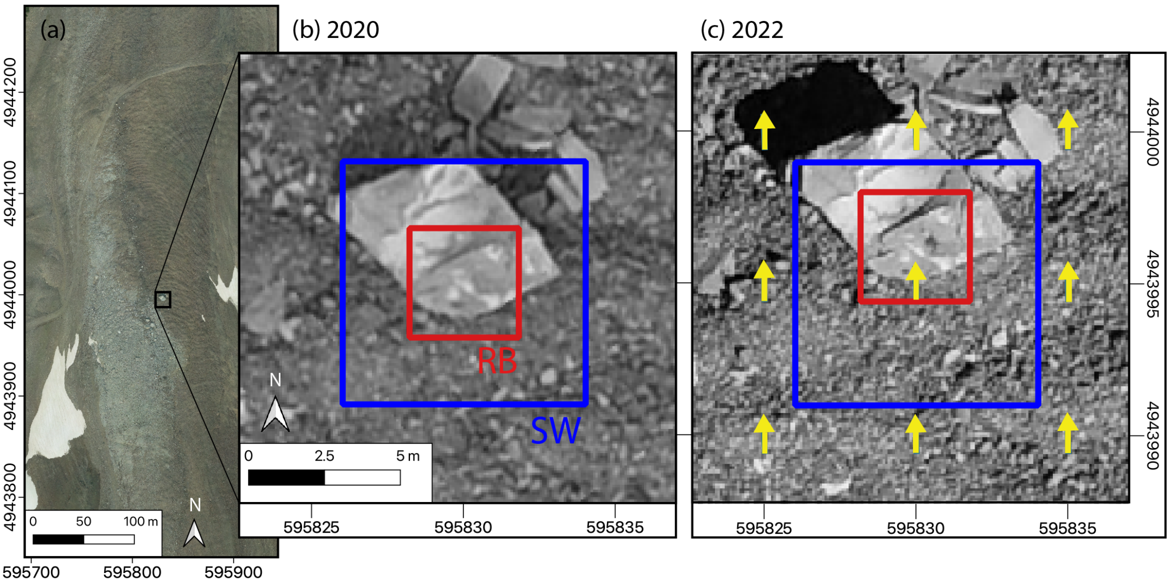

Figure 2. Schematic of the change detection procedure applied to a boulder identified at a central location in the August 2020/August 2022 image pair at Galena Creek (**a**), where the red box labeled RB represents the 45 × 45 pixel reference block and the blue box labeled SW represents the 100 × 100 pixel search window. The movement of RB between 2020 (**b**) and 2022 (**c**) shows the displacement measured as the location of the peak normalized correlation coefficient within the search window. The yellow arrows represent the two-year displacement vectors measured by CIAS; this boulder moved approximately 1.2 m at an azimuth of 358°.

The change detection process was then performed again, this time using the shifted SkyMap50 image with its corresponding unshifted image partner. Its results were verified by manually examining off-glacier stationary features in both the unshifted and shifted images for each pair containing a SkyMap50 scene. The new change detection results were compared with the initial results of the unshifted images after subtracting the mean displacement of the stationary subset for further verification and uncertainty analysis. The added step of translating the second image of the pair, along with the relatively lower resolution of the SkyMap50 imagery (42 $\frac{\text{cm}}{\text{pixel}}$) compared with the drone imagery (<10 $\frac{\text{cm}}{\text{pixel}}$), leads to a higher uncertainty in those surface displacements estimated with pairs containing a shifted satellite image.

Table 2. Static shift applied to the SkyMap50 images to minimize the measured displacement of stationary terrain in each image pair.

Rock Glacier	Image 1	Image 2	Δx (m E)	Δy (m N)
Galena Creek	10 July 2021 ^{S*}	8 August 2022 ^{U}	−0.99	−1.20
Sulphur Creek	10 July 2021 ^{S}	7 August 2022 ^{S*}	0.84	−1.25
Sulphur Creek	25 August 2020 ^{A}	7 August 2022 ^{S*}	0.81	0.68

^{U} UAS image; ^{A} Piloted airborne image; ^{S} SkyMap50 satellite image; * Denotes that the image was shifted relative to the other image in the pair.

2.3. Surface Elevation Change

For the UAS and airborne datasets, the photogrammetric processing workflow produces DEMs with pixel widths twice those of their corresponding orthomosaics (Supplementary Figure S1); thus, the DEMs used in this study range from approximately 10–50 $\frac{\text{cm}}{\text{pixel}}$. Using these elevation maps, we calculated the surface elevation changes for Galena Creek, Sourdough, and McCarthy Creek over the time intervals between the earliest and latest photogrammetric acquisitions in order to observe any detectable signatures of horizontal flow or vertical thinning. For Galena Creek, the elevation change was calculated over the

August 2020/August 2022 interval; for Sourdough, the May 2014/July 2022 interval was used; and for McCarthy Creek, the May 2020/June 2021 interval was used. All of these elevation differences were calculated by subtracting the earlier DEM from the later DEM in each pair using the *Raster Calculator* tool in QGIS with the coarsest-resolution DEM as the reference.

To examine the surface change at Sulphur Creek, we calculated the difference between the DEM produced by the August 2020 airborne photogrammetry flight and the $\frac{1}{3}$ arcsecond resolution (approximately 10 m) DEM tile from the USGS 3D Elevation Program (3DEP) [41]. The spatial metadata for this tile indicate that the 3DEP data at Sulphur Creek was sourced from topographic information measured in 1985. Because this location in the 3DEP dataset is mostly barren land, the error of this $\frac{1}{3}$ arcsecond DEM is estimated to have a mean bias of -0.85 m with a standard deviation of 2.42 m [42]. We consider this bias in the data when interpreting the elevation change results discussed below.

3. Results

3.1. Wyoming

3.1.1. Galena Creek

At Galena Creek, the August 2020/August 2022 image pair resampled to 8.0 $\frac{\text{cm}}{\text{pixel}}$ resolution provided the best change detection signal in the set of image pairs. Surface displacement is detectable along the main trunk of the rock glacier, in contrast to the adjacent stationary terrain (Figure 3b). The displacements have a strong correlation with the surface slope, indicating a direct relationship between driving stress and flow velocity. The change detection algorithm cannot measure displacements on surface regions when there is snow in one or both of the images due to the low contrast and lack of pixel correlation within the reference block. These regions cause "noisy" results, which are identifiable in the mapped displacement vectors as regions with random displacement vector magnitude and direction that are associated with the snow patches when the displacement vectors are mapped over the base images. The effect of these noisy regions on the analysis of the data is mitigated by ignoring the displacement vectors greater than a noise threshold, which is determined by visually evaluating the flow field to find the maximum displacement with a direction that agrees with the local topography. For the case of Galena Creek, this threshold is approximately 1.6 $\frac{\text{m}}{\text{yr}}$. The noise may be further filtered by ignoring vectors where the displacement direction differs from the slope azimuth by more than 45°. The minimum displacement error for each image pair is taken to be the greater value of either the minimum displacement over a region interpreted to be stationary or the pixel size of the images. Using these metrics, a pair of low-altitude UAS images acquired with the same camera and positioning system for both surveys returned the best displacement measurements out of all the datasets presented here.

The photogrammetry data collected at Galena Creek allowed us an opportunity to directly compare the efficacy of the change detection method using imagery from homogeneous and heterogeneous platforms. We performed a hybrid change detection experiment using the 42 $\frac{\text{cm}}{\text{pixel}}$ SkyMap50 satellite image from July 2021 and the August 2022 UAS image resampled to 42 $\frac{\text{cm}}{\text{pixel}}$ with the cubic spline method. The displacement patterns in the upper two-thirds of the rock glacier are similar between the homogeneous change detection results and the hybrid results. The magnitude of the displacement is directly correlated with the surface slope (Figure 3c); however, the coarser resolution of the satellite image in the lower third of the rock glacier means that the proportion of mismatches and undetected movements increases due to the increased difference in pixel size between the original UAS and satellite images [43].

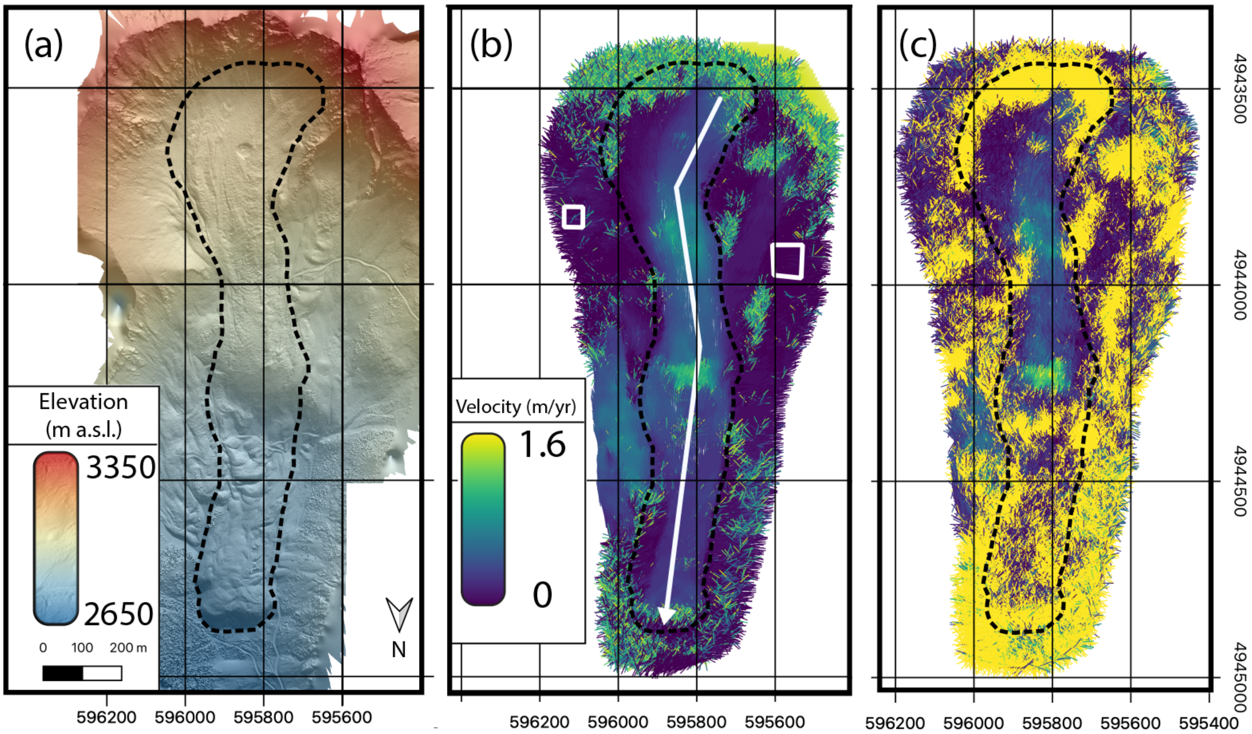

Figure 3. Galena Creek photogrammetry results: (**a**) DEM and hillshade produced from the August 2022 UAS flight; (**b**) surface velocity field derived from change detection between the August 2020 and August 2022 UAS-derived orthomosaics; (**c**) surface velocity field derived from change detection between the shifted July 2021 satellite image and the August 2022 orthomosaic. For reference, the extended rock glacier outline is delineated as a dashed line in each panel, the white line in (**b**) marks the profile that was sampled for the age analysis discussed below, and the white boxes in (**b**) indicate the stable points used in the uncertainty analysis.

3.1.2. Sulphur Creek

We detected a flow signal on the Sulphur Creek surface (Figure 4) using the August 2020 airborne imagery combined with the August 2022 SkyMap50 image, which was linearly shifted to account for the co-registration error between the two images (Table 2). Although the displacement values on the stable surfaces of the rock glacier surface indicate a relatively high baseline uncertainty, there is a signal of increased flow velocity on the lowest lobe of the rock glacier. In contrast, there does not appear to be substantial downslope movement in the middle portion of the rock glacier, where GPR and geomorphic observations indicate ice thicknesses of less than 10 m and stagnation of the ice [31,37].

These change detection results support the hypothesis of ice stagnation on a deflating debris-covered glacier that is transitioning to dead ice. The directions of the displacement vectors on this central portion of the glacier agree with the slope aspect (approximately 150°), suggesting movement toward the middle line of the glacier. This movement may be an effect of rapid recent thinning by incision of a supraglacial stream and subsequent ice flow from the thicker ice at the glacier margins to the thinned ice in the middle (see the elevation change results in Section 3.3). Alternatively, if the thinning is concentrated along a longitudinal line associated with a stream in the center of the glacier, this could lead to a reduction in the cross-flow buttressing force, allowing the lateral portions of the glacier to cohesively slide along the base towards the central trough. With either mechanism, this downwasting appears to preserve the surface debris structure, as the change detection algorithm successfully tracks features in the region over a spatial scale of a few hundred meters.

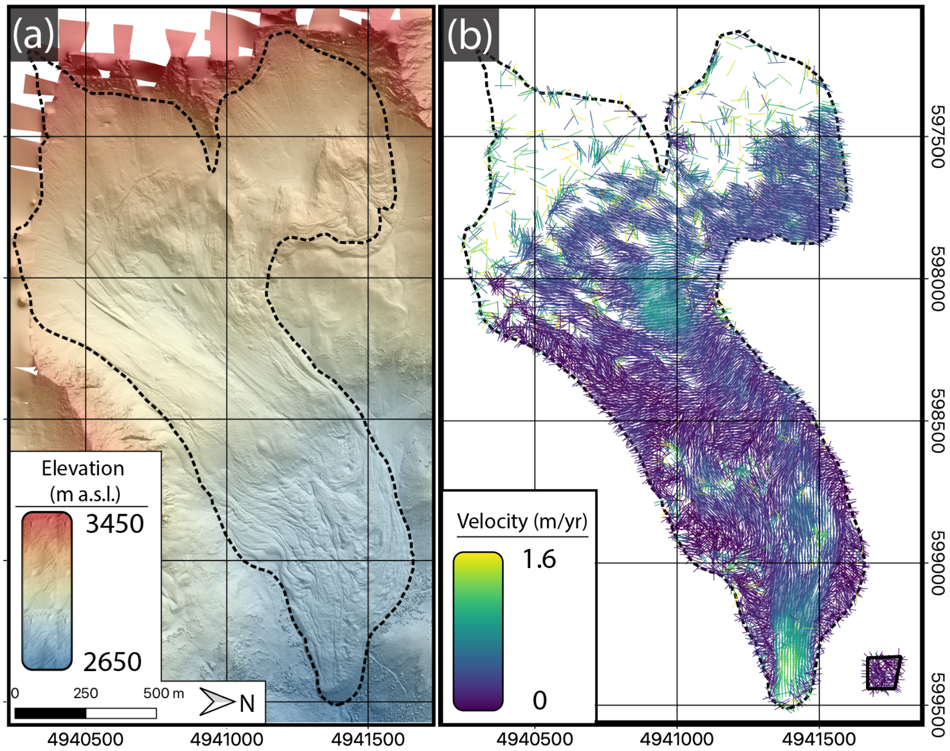

Figure 4. Sulphur Creek photogrammetry results: (**a**) DEM and hillshade produced from the August 2020 piloted overflight and (**b**) surface velocity field derived from change detection between the August 2020 airborne orthomosaic and the shifted August 2022 satellite image. For reference, the extended rock glacier outline is delineated as a dashed line in each panel. The box in the lower right corner of (**b**) indicates the stable area used for the uncertainty analysis.

3.2. Alaska

3.2.1. Sourdough

The data at Sourdough represent the longest monitoring period of the sites presented here, spanning from May 2014 to July 2022 (Figure 5, Table 1). To characterize the temporal variations in the flow field, we calculated surface displacements for image pairs from adjacent years (Figure 6) and the progressive displacement for subsequent images with respect to the May 2014 initial image. All of the annual image pairs show a consistently fast-moving region with distinct shear margins on the lower trunk of the rock glacier flowing at rates greater than 1 $\frac{\text{m}}{\text{yr}}$ (Figure 6), indicating a high level of rock glacier activity. We ignore velocity vectors with magnitudes greater than 1.8 $\frac{\text{m}}{\text{yr}}$, as visual examination indicates that all greater values are qualitative outliers with no directional correlation to the surrounding data points. These spurious velocity vectors are considered noise due to mismatched pixel blocks in the change detection routine. The resulting velocity maps distinguish an active secondary lobe that branches southeast from the main trunk after flowing around a bedrock pinning point. Below this pinning point, the flow of the main trunk and secondary lobe diverges and slows as the slope flattens, creating the characteristic tongue-shaped lobes of the lower rock glacier. Stagnant overflow lobes with low displacements are observed along the west edge of the feature (Figure 1a). While these flow patterns are evident when observing the full set of image pairs with intervals of one year or greater; the results of individual image pairs vary in quality, making it difficult to asses possible seasonal signals in the flow field.

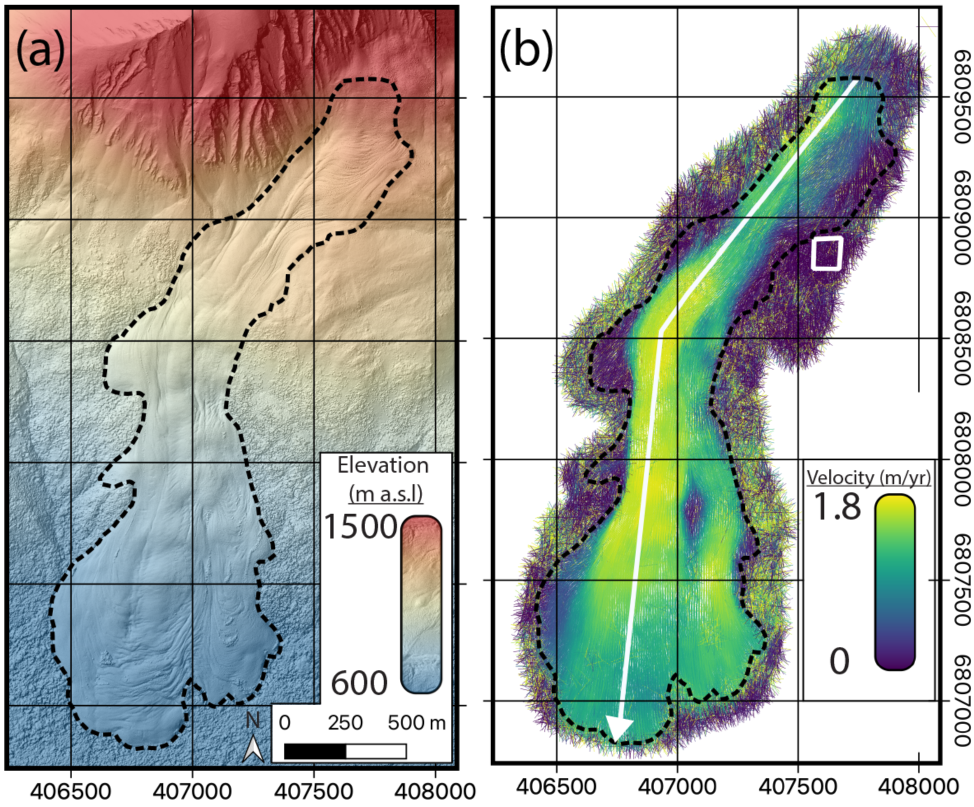

Figure 5. Sourdough photogrammetry results: (**a**) DEM and hillshade produced from the May 2014 piloted overflight and (**b**) surface velocity field derived from change detection between the May 2014 and September 2019 airborne orthomosaics. For reference, the extended rock glacier outline is delineated as a dashed line in each panel, the white line in (**b**) marks the profile that was sampled for the age analysis detailed below, and stable area used for the uncertainty analysis is marked by the white box in (**b**).

The displacement signal is generally stronger in the image pairs with longer time intervals. This indicates that larger displacements are detected more readily and consistently as long as the search window is large enough to contain the range of realistic displacements. The image pair with the greatest amount of noise is the September 2019/October 2020 interval; this noise is largely correlated with the presence of snow on the upper two-thirds of the rock glacier in the October 2020 image. This snow obscures surface features, which leads to inconsistencies in pixel intensity patterns, causing the normalized cross-correlation algorithm to fail. The remaining image pairs with annual time intervals exhibit a consistent pattern of increased surface velocity in the trunk of the rock glacier, although these results have varying degrees of signal and noise. To estimate the total displacement and average velocity of the rock glacier surface over the entire measurement period, we measured the displacement for all of the images as referenced to the May 2014 image (Supplementary Figure S2). This method successfully detects a peak velocity of approximately 1.5 $\frac{\mathrm{m}}{\mathrm{yr}}$ in the central trunk of the rock glacier; however, comparing the results from images acquired at different times of year does not reveal any surges or seasonal signals in the velocity field. Shorter time intervals between acquisitions and imagery with increased spatial resolution paired with permanent GNSS stations on the rock glacier's surface could shed further light on its seasonal flow patterns [44].

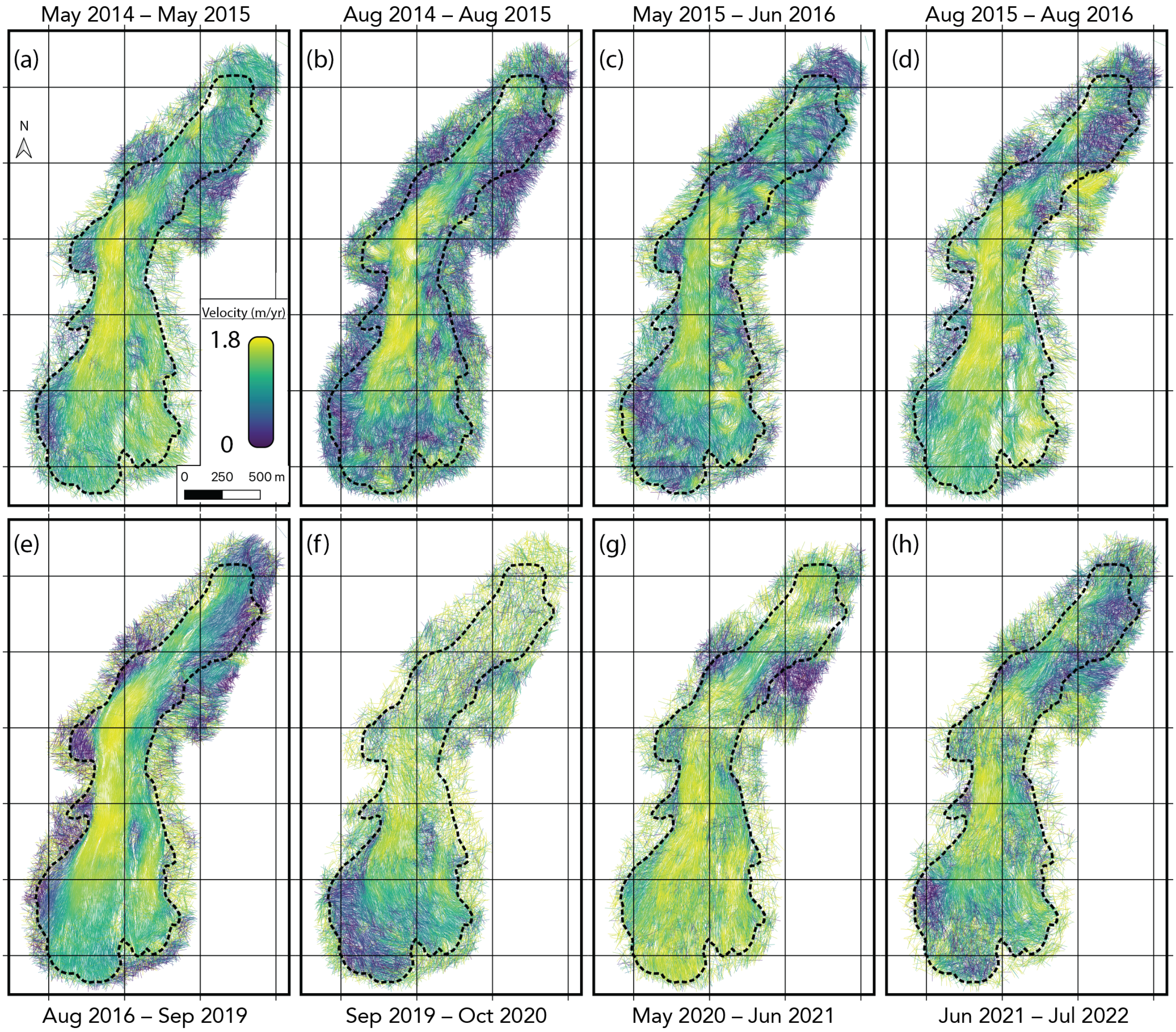

Figure 6. Surface velocity results for Sourdough using image pairs with time intervals of one year or more, demonstrating the range in quality of the change detection results for different image pairs and time intervals. The grid used for these maps is equivalent to the grid used in Figure 5, where the grid lines are drawn at 500 m intervals in the x and y directions in the projected coordinate system. Each panel (**a**–**h**) shows the results from image pairs, progressing in chronological order.

3.2.2. McCarthy Creek

The results at McCarthy Creek are generally noisier than at Sourdough, and the change detection results for the entire measurement period at McCarthy Creek show a flow pattern with a maximum velocity approximately half that of Sourdough (Figure 7). We chose to use the August 2014 image as the base image for the McCarthy Creek analysis because there was lingering snow on the upper portion of the rock glacier in the May 2014 image, meaning that the August 2014 image was able to detect a flow signal at higher reaches of the rock glacier. The fastest section of the rock glacier surface is the southern/upstream portion of its trunk, moving about 50 $\frac{\text{cm}}{\text{yr}}$, before slowing as the flow of the lower lobe diverges. At approximately 1200 m elevation the rock glacier branches into a fast southern lobe and a more stagnant northern lobe.

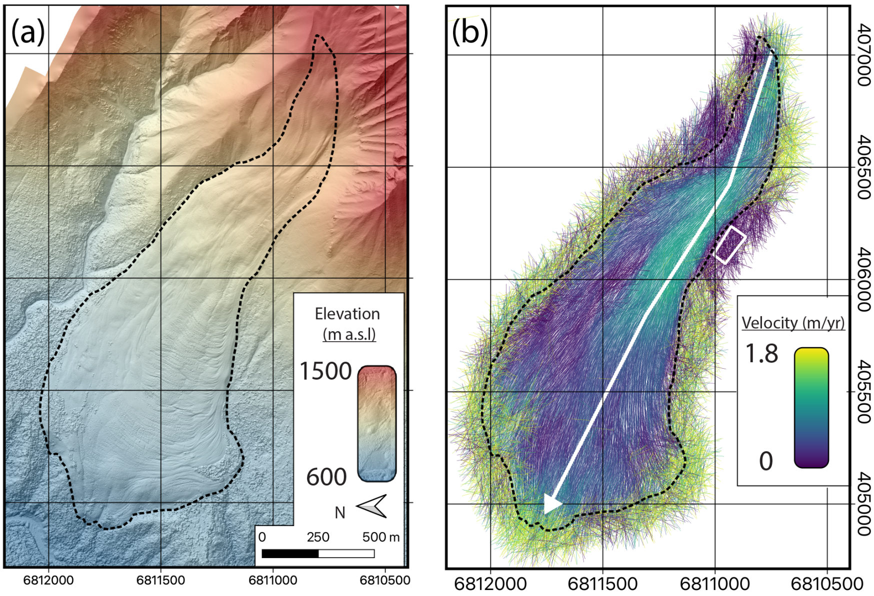

Figure 7. McCarthy Creek photogrammetry results: (**a**) DEM and hillshade produced from the May 2014 piloted overflight and (**b**) surface velocity field derived from change detection between the August 2014 and June 2021 airborne orthomosaics. For reference, the extended rock glacier outline is delineated as a dashed line in each panel, the white line in (**b**) marks the profile that was sampled for the age analysis below, and the stable area used for the uncertainty analysis is marked by the white box in (**b**).

There appears to be an increase in flow speed at the toe of the rock glacier, which could indicate a recent frontal advance or an increase in wasting and potential collapse of the rock glacier toe near the river channel of the McCarthy Creek drainage. However, this apparent signal could alternatively be caused by the combined geometric effects of the photogrammetric data acquisition, the surface slope at this location, and/or uncertainty due to vegetation on the surface. Similar to Sourdough, the change detection at McCarthy Creek performs the best for time intervals greater than one year, and the signal is generally stronger for longer time intervals (Figure 8). In Section 4.2, we discuss the estimation of the baseline uncertainty in these change detection results and how this affects further analysis and interpretation of the data.

3.3. Surface Elevation Change

At Galena Creek, subtracting the earlier DEM from the later DEM reveals indicators of both vertical thinning and surface-parallel motion (Figure 9a). There is an apparent bias of approximately -20 cm between the two DEMs, as shown by differencing the elevations of stable terrain. The elevation difference measured along a longitudinal profile on the rock glacier surface indicates a mean DEM difference of -40 cm with a standard deviation of 19 cm. By comparison, a sample of DEM differences on the stable ground provides a mean value of -18 cm with a standard deviation of 6 cm. A cross-flow profile of the elevation differences supports this observation as well (Supplementary Figure S3). This suggests that the rock glacier surface has lowered by 22 ± 13 cm over the two-year time interval. This 10 $\frac{\text{cm}}{\text{yr}}$ thinning rate for the upper two-thirds of the rock glacier agrees with previous estimates [12,38]. This thinning rate measurement further agrees with a thermal conduction model using air temperature data from the *Evening Star* Snowpack Telemetry (SNOTEL) meteorological station located <1 km east of Galena Creek at a similar elevation as the rock glacier's terminus (station ID = 472). This model uses an observed supraglacial debris thickness of 1.5 m [31], and the measured thinning rate fits a plausible range of thermal conductivities for the debris (Appendix A). The ice in the cirque of Galena Creek has a

GPR-measured thickness of >50 m; thus, assuming that this interpreted thinning rate of 10 $\frac{\text{cm}}{\text{yr}}$ remains constant, the glacial ice will be preserved here past the year 2500.

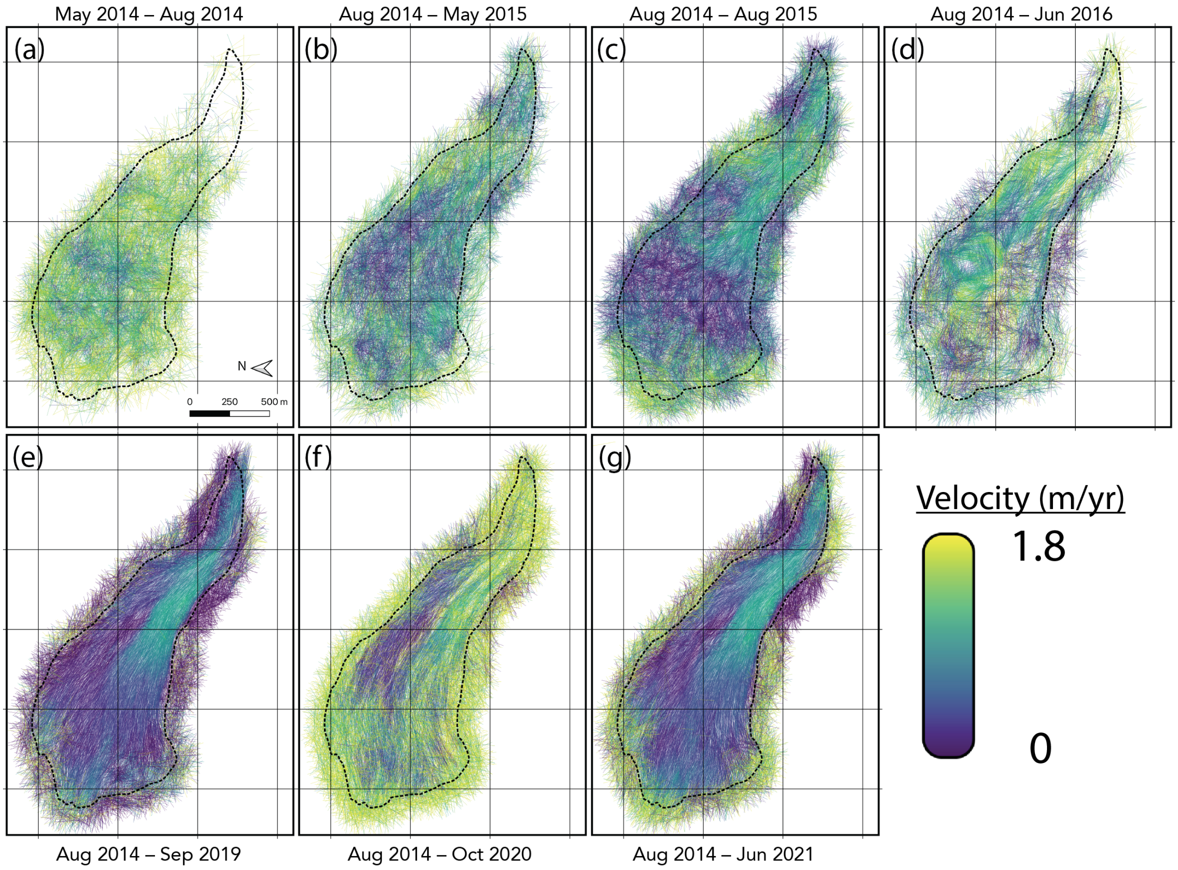

Figure 8. Surface velocity results for McCarthy Creek using image pairs, where each labeled panel was derived in reference to the August 2014 base image, demonstrating the general increase in quality of the change detection results at McCarthy Creek with increasing surface displacement while showing the impact of snow in the October 2020 image. The grid used for these maps is equivalent to the grid used in Figure 7, where the grid lines are drawn at 500 m intervals in the x and y directions in the projected coordinate system. Each panel (**a**–**g**) shows the results where images are chronologically compared to the August 2014 base image.

In addition to the overall thinning of the upper two-thirds of the rock glacier, flow-parallel oscillations in the DEM difference rasters are indicative of the translational motion of surface ridges/furrows, creating a positive value where a ridge has occupied previously void space and a negative value where a furrow has replaced a ridge. The distances between these troughs and crests in the oscillations of the DEM difference data are comparable with the surface displacement measured over the same period. Furthermore, strong negative values within the rock glacier boundaries appear to correlate with a sub-debris supraglacial creek that has been observed to expose ice to the surface. This observation suggests that ablation is concentrated in regions where ice has been exposed to the atmosphere due to the mass wasting of debris by supraglacial melt. These results exemplify the utility of high-resolution photogrammetry data in resolving cm-scale elevation changes on rock glacier surfaces from year to year.

To estimate the surface elevation change at Sulphur Creek, we calculated the difference between the $\frac{1}{3}$ arcsecond resolution (about 10 m/pixel) USGS 3DEP DEM surveyed in 1985 [41] and the 2020 airborne-derived DEM. The surface elevation change appears to be biased towards surface lowering, with a 0.315 km^2 section interpreted to be stable ground showing a mean difference of -4.9 ± 3.5 m, with the error here represented as one standard deviation. However, three regions in the Sulphur Creek image display surface lowering that exceeds the bias in the difference calculated between the 1985 and 2020 DEMs. The first region (labeled "1" in Figure 9b) has a surface area of 0.072 km^2 and displays a mean surface elevation change of -18.3 ± 4.1 m. Region 1 in this map corresponds with the region exhibiting inward flow in the change detection results, and the combination of these observations suggests rapid stagnation and collapse of the middle section of Sulphur Creek, supporting the interpretation of [37]. Region 2 has a surface area of 0.085 km^2 with -23.9 ± 3.5 m of surface change, while Region 3 has a surface area of 0.141 km^2 with -27.9 ± 5.9 m of surface change.

Regions 2 and 3 correspond with the two small cirque glaciers occupying the two forks of the upper Sulphur Creek basin. Accounting for the bias in elevation change estimated from the off-glacier terrain, Regions 1, 2, and 3 of Sulphur Creek have experienced mean thinning rates of $38 \pm 12\ \frac{\text{cm}}{\text{yr}}$, $54 \pm 10\ \frac{\text{cm}}{\text{yr}}$, and $66 \pm 17\ \frac{\text{cm}}{\text{yr}}$, respectively, over the 35-year DEM interval. These thinning rates indicate significant recent negative mass balance for the higher-elevation components of the Sulphur Creek system. We applied our simple thermal model here using a debris thickness of 0.5 along with SNOTEL data spanning the years 1990–2020; this model supports the result that Sulphur Creek has lost upwards of 20 m of ice to cumulative melt under a reasonable range of thermal conductivities for the debris (Appendix A). At these melt rates, the Sulphur Creek basin may lose the entirety of its glacial ice before 2100, and the only remaining subsurface ice in this basin will be preserved in an ice-cemented rock glacier. Future Wyoming fieldwork should aim to collect a UAS-derived DEM at Sulphur Creek to measure surface elevation change after the acquisition of the 2020 dataset and compare the results with the 1985–2020 surface elevation change rates as well as with the results from the neighboring Galena Creek.

In contrast to the Wyoming sites, the surface change between the earliest and latest datasets for the Alaska sites does not suggest broad patterns of elevation increase or decrease across the entirety of each rock glacier. Stationary regions near the rock glacier margins show a mean systematic bias of about +40 cm for the May 2014/July 2022 DEM pair for Sourdough (Figure 9c) and about +30 cm for the May 2014/June 2021 DEM pair for McCarthy Creek (Figure 9d). The mean systematic biases have corresponding standard deviations of about 50 cm for both rock glaciers. This estimate is complicated by the dense vegetation surrounding much of the rock glaciers' perimeters, meaning that stable bedrock estimations must be taken from locations with steep slopes, where the DEM error is likely the highest. There is not a clear change in the mean surface elevation change on either rock glacier surface compared to the surrounding stable terrain in the photogrammetric DEMs when compared with one another or when compared with the corresponding USGS 3DEP product. However, these elevation change results are similar to the Galena Creek results in that the variability of the surface change increases on the surface of the rock glaciers as opposed to off-glacier locations. This variability appears to be an effect of the translational motion of surface ridges and furrows, as the topographic oscillations are oriented perpendicular to flow while their wavelengths and velocities are generally out of phase with the timing of the data acquisition.

The translational motion of ridges can be observed by plotting elevation profiles from multiple flights. These profiles show that any thickness changes of the rock glacier are less than the vertical uncertainty in the elevation data, which is on the order of a few decimeters (Supplementary Figures S4 and S5). At Sourdough, there is a region of apparent thinning in its uppermost reaches corresponding with debris and avalanche cones, as well as a broad region of negative elevation change about 200 m wide on the lower lobe. The elevation change variability in the trunks of the Alaskan sites may include localized thinning that falls within the uncertainty of the elevation data; however, neither of the Alaskan sites indicate broadly consistent thinning across the surface. This result is supported by the thermal conduction model described in Appendix A. Localized elevation gain is observed near the toe of Sourdough as a result of its terminus advancing, which is corroborated by field observations of "bulldozed" trees.

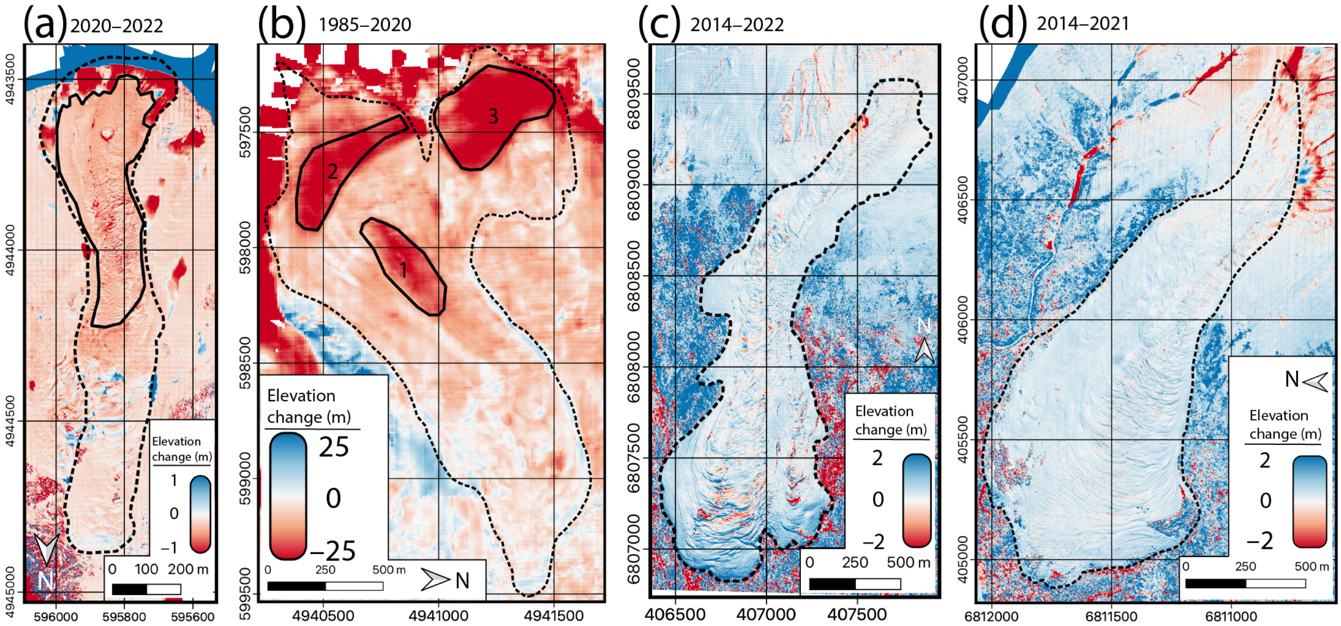

Figure 9. Surface elevation change results: (**a**) the August 2020/August 2022 UAS DEM pair for Galena Creek, with the region of increased ablation outlined in the solid black line; (**b**) the 1985 DEM from USGS 3DEP paired with the August 2020 airborne DEM for Sulphur Creek, where the regions labeled 1, 2, and 3 indicate areas of high thinning rates; (**c**) the May 2014/July 2022 airborne DEM pair for Sourdough; (**d**) the May 2014/June 2021 airborne DEM pair for McCarthy Creek.

In general, all of our rock glacier surface change maps exhibit indicators of longitudinal flow in agreement with the optical change detection results. Further, the Wyoming sites demonstrate clear signals of vertical thinning due to ice melt, with Sulphur Creek experiencing the fastest melt rate. The Alaska sites do not exhibit the same thinning signals. These trends are consistent with a thermal conduction model (Appendix A) using GPR-derived debris thickness measurements that show the debris to be thinnest at the upper part of Sulphur Creek and thickest at Sourdough [31]. Assuming similar mean annual air temperatures and constant thermal conductivities for the debris at all four sites, it is expected that the thinner debris at Sulphur Creek would lead to the highest melt rate, while the thick debris at the Alaska sites would inhibit melt to a greater degree. In the following section, we discuss the implications of these surface change results for the accumulation and evolution of each of these field sites; in addition, we further consider the sources of uncertainty in these results by defining criteria for assessing the accuracy of the horizontal and vertical surface change products.

4. Discussion

4.1. Validation and Uncertainty Analysis

The image pair collected with the UAS in both August 2020 and August 2022 shows a baseline velocity uncertainty of 6.8 $\frac{\text{cm}}{\text{yr}}$ (Table 3). This is the average value of the displacements returned from a subset of the CIAS results consisting of 320 points where bedrock is assumed to be motionless (Figure 3b). Examining the means of the vector components and their standard deviations provides information about the sources of uncertainty [45]. The mean x and y components of the UAS-derived velocity measurements at Galena Creek show that the systematic error is less than 1 cm. The standard deviations indicate that the random error is uniform in both directions and is comparable to the pixel size of the image. These values are similar to the results of photogrammetric change detection surveys in the Swiss Alps [46]. In comparison, the image pair using the coarser satellite image returned much higher uncertainty values due to the increase in mismatches leading to more noise in the results. Using repeated surface-based position measurements of marked boulders at Galena Creek, we validate our change detection results with independent velocity measurements in consideration of the uncertainty of our remote sensing results. We compare the velocities measured from boulder positions in 2015 and 2022 with the four nearest UAS-derived velocity values over the 2020 to 2022 interval [38].

Table 3. List of image pairs used for velocity measurements and the associated velocity uncertainties measured using regions of stable terrain at each field site. All means and standard deviations reported here are provided in units of $\frac{\text{m}}{\text{yr}}$.

Site	Stable Terrain Area (m^2)	# of Points	Image Pair	Mean ($\lvert v \rvert$)	Mean (v_x)	Mean (v_y)	$\sigma(v_x)$	$\sigma(v_y)$
Galena Creek	8400	320	August 20 August 22	0.068	0.009	−0.006	0.109	0.103
	8400	320	July 21 August 22	5.65	−0.290	0.018	6.43	7.11
Sulphur Creek	11,550	111	August 20 August 22	0.104	0.010	−0.010	0.112	0.086
Sourdough	13,600	141	May 14 August 14	1.11	0.948	−0.011	0.877	0.519
	13,600	141	May 14 May 15	0.246	−0.147	0.029	0.229	0.106
	13,600	141	May 14 August 15	0.288	0.163	0.017	0.336	0.349
	13,600	141	May 14 June 16	0.208	−0.171	0.070	0.118	0.059
	13,600	141	May 14 August 16	0.466	−0.345	−0.250	0.114	0.198
	13,600	141	May 14 September 19	0.057	0.014	0.003	0.063	0.134
	13,600	141	May 14 May 20	0.105	−0.034	0.001	0.234	0.235
	13,600	141	May 14 October 20	0.259	−0.091	−0.112	0.356	0.373
	13,600	141	May 14 June 21	0.042	−0.004	−0.038	0.014	0.019
	13,600	141	May 14 July 22	0.091	−0.014	−0.051	0.135	0.154
McCarthy Creek	11,030	111	May 14 August 14	6.64	2.02	0.293	8.30	6.17
	11,030	111	August 14 May 15	0.470	0.006	0.018	0.612	0.721
	11,030	111	August 14 August 15	0.403	0.046	0.067	0.407	0.327
	11,030	111	August 14 June 16	1.31	−0.231	0.201	1.41	1.21
	11,030	111	August 14 September 19	0.086	0.033	0.004	0.235	0.155
	11,030	111	August 14 October 20	1.06	−0.043	−0.140	0.952	0.855
	11,030	111	August 14 June 21	0.078	0−0.021	−0.018	0.086	0.146

In the upper section of Galena Creek, the change detection and boulder position results are in good agreement, with a maximum velocity magnitude difference of about 5 $\frac{\text{cm}}{\text{yr}}$, similar to the baseline uncertainty in the August 2020/August 2022 CIAS results (Figure 10). On the lower third of the rock glacier, four measurements show a discrepancy of 10 $\frac{\text{cm}}{\text{yr}}$ or greater between the 2015–2022 boulder measurements and the 2020–2022 change detection measurements. The largest of these discrepancies (0.36 $\frac{\text{m}}{\text{yr}}$) can be explained by noise in the change detection data, where a patch of trees created a zone of mismatched pixel clusters at the location of the surface measurement. The three other points with discrepancies greater than 5 cm exhibit an anisotropic bias, where the change detection measurements are about 10 $\frac{\text{cm}}{\text{yr}}$ faster than the boulder point measurements; most of the variation occurs along the y-axis. This could indicate a rapid acceleration of the lower rock glacier lobe by 10 $\frac{\text{cm}}{\text{yr}}$ between 2015 and 2020, or could be an effect of errors in measurement and the coordinate system transformation of the boulder positions on this lower lobe between the 2015 and 2022 surveys. A coordinate rotation was applied to the 2015 points, and the boulders on the lower lobe are the most distant from the pole of rotation, making them the most susceptible to an error in the rotation angle between coordinate systems. The deviation between boulder displacements and CIAS results generally increases when using boulder position measurements from 1997 to 1999 (Supplementary Figure S6), which may be an effect of either a changing rock glacier surface velocity field or a decreased measurement error with newer global positioning technology.

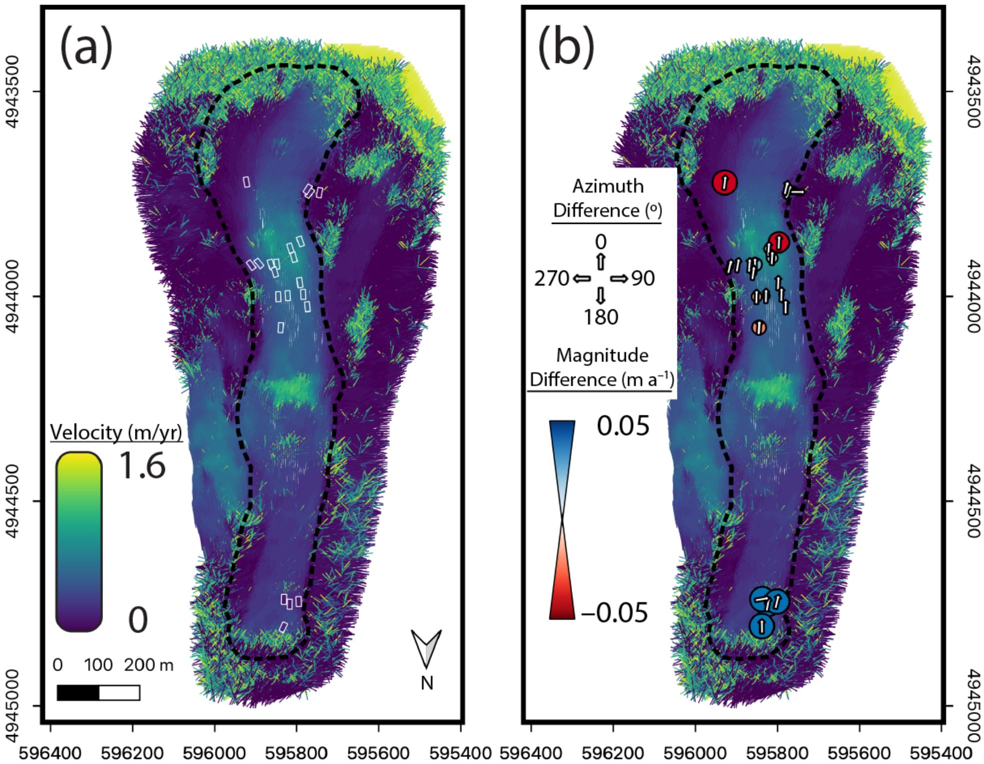

Figure 10. Comparison of photogrammetric change detection results between August 2020 and August 2022 UAS imagery with boulder velocities between August 2015 and August 2022 at Galena Creek. (**a**) The boulder velocity vectors are shown as rectangles with white borders, color-coded according to velocity magnitude and oriented according to the vector's direction; these boulder velocities are plotted over the automated change detection results using the same color scale. (**b**) The difference in magnitude and azimuth between the measured boulder velocities and the four nearest grid points in the change detection measurements. The size and color of each dot in (**b**) corresponds to its magnitude and sign and the direction of the arrow indicates the difference in vector azimuth, meaning that vectors with no change in azimuth display an arrow that faces directly upwards.

Although the airborne photogrammetry at the Alaska sites provides a clear signal of flow on both rock glaciers, uncertainty estimation using stable bedrock points is complicated by forest cover surrounding most of the perimeters of Sourdough and McCarthy Creek. The seasonally changing tree canopy provides poor references for the change detection algorithm, and this leads to mismatched and noisy results immediately surrounding the rock glacier. As we have no repeated surface-based boulder measurements for the Alaska sites, we examine the uncertainty in our change detection measurements here using two metrics: the range of peak velocities across a transverse profile, and the average minimum velocity on stable ground.

The first measure used to characterize the velocity uncertainty for the change detection results is the range in the magnitude of the peak velocities measured along a common transverse profile on the rock glacier surface for all of the time intervals examined. This range is about 0.4 $\frac{\text{m}}{\text{yr}}$, though this variability estimation may contain variations in the rock glacier's true velocity field during the measurement period. The second quantification of the uncertainty in measured velocity for each image pair is calculated by averaging a subset of low-magnitude displacement vectors selected at regions of the image interpreted to be bare stable ground. This value represents the minimum apparent velocity between stationary points in two images; therefore, we take these values as a representation of the uncertainty for the on-glacier velocity.

The averaged minimum velocity magnitudes of stable terrain are variable for the Sourdough image pairs, generally varying around a value of approximately 20 $\frac{\text{cm}}{\text{yr}}$. There is a trend of decreasing uncertainty with increasing time interval between image, though other factors such as a warped orthomosaic (August 2016) or a snow-covered surface (October 2020) contribute to these uncertainty values. Because the standard deviations of the vector components are generally random random, showing that there is no directional bias to these minimum velocity values, the value of ±20 $\frac{\text{cm}}{\text{yr}}$ (total range of 40 $\frac{\text{cm}}{\text{yr}}$) agrees with the range of 40 cm measured from the difference between the velocity peaks along a common profile for all image pairs. Therefore, we assume the random error in the Alaskan airborne datasets to be approximately ±20 $\frac{\text{cm}}{\text{yr}}$, while the systemic error approaches values less than 5 $\frac{\text{cm}}{\text{yr}}$, especially for longer time intervals.

Systematic biases likely exist in local regions of the individual image pairs. For example, in the May 2020/June 2021 image pair, the lower lobe of the rock glacier exhibits a velocity magnitude much greater than the magnitudes at the same area in the other image pairs, where the velocity decreases with proximity to the terminus (Figure 6). We suggest that this systematic bias in the May 2020/June 2021 image pair results from effects in the photogrammetric processing step, which could have led to geometric warping of the orthomosaics. The processing reports generated by the Agisoft Metashape software indicate that these two images had the highest percentage of regions on the rock glacier where the image overlap was less than nine (see the supplementary materials for the processing reports), which supports the hypothesis that the systematic error in this image pair is due to artifacts from the photogrammetric processing. Additionally, nonzero means of stable terrain velocity magnitudes combined with unequal standard deviations are indicative of systematic and/or nonuniform uncertainty distributions, such as that of the May 2014/June 2016 image pair at Sourdough (Table 3). Future studies should visually identify regions that may contain warping of the orthomosaic and the associated increase in uncertainty in order to avoid misinterpretation of the physical implications of the velocity field.

To further understand the relative quality of the change detection results for different image pairs, we examined the distributions of output velocities and maximum correlation coefficients for Sourdough and Galena Creek. We used the eight image pairs at Sourdough to examine the characteristics of velocity and correlation coefficient distributions. Qualitatively, one way to compare velocity measurements for different image pairs is to compare the tails of the distribution, where the output velocity is greater than the highest expected real velocity (about 2 $\frac{\text{m}}{\text{yr}}$ for Sourdough). For example, the August 14/August 2015 results for Sourdough have fewer outlying velocity values than those for May 14/May 15 (Figure 11). In Figure 6, it can be observed that the velocity field for August 2014/August 2015 has a lower baseline uncertainty than for May 14/May 15, leading to the conclusion that the quality of the results can partially be characterized by the number of outlying velocity magnitudes. These observations can be used to weight the velocity vector fields of specific image pairs during future kinematic analyses.

The distributions of the maximum correlation coefficients output by the CIAS algorithm provide another assessment of the reliability of the results for each image pair. These histograms (Figure 12) show a relationship between the width of the distribution of the maximum correlation coefficients and the quality of the change detection results. Two of the highest quality velocity fields as assessed by baseline uncertainty and flow signal continuity are August 2014/August 2015 and August 2016/September 2019. These two image pairs return the narrowest distribution of the maximum correlation coefficients. On the other hand, May 2014/May 2015 and September 2019/October 2020 have relatively low quality results, and broader distributions of the maximum correlation coefficients are observed. This effect is especially apparent for the September 2019/October 2020 pair.

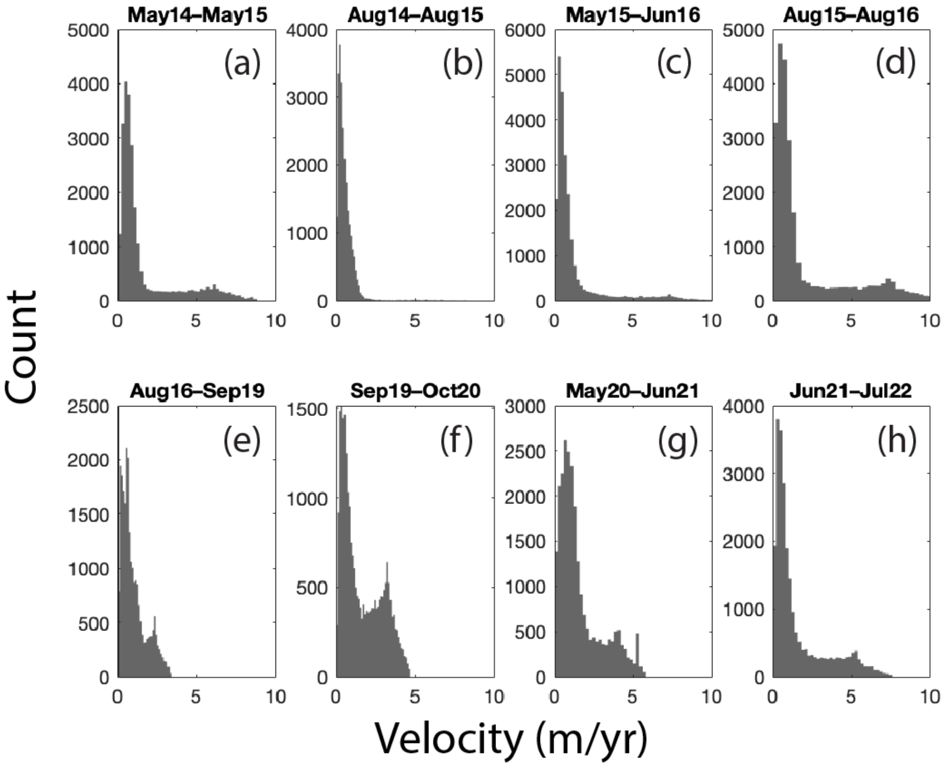

Figure 11. Histograms showing the distribution of velocity magnitudes for each image pair at Sourdough with a time interval of one year or longer. Each panel (**a**–**h**) corresponds with the results presented in the same panel labeled in Figure 6.

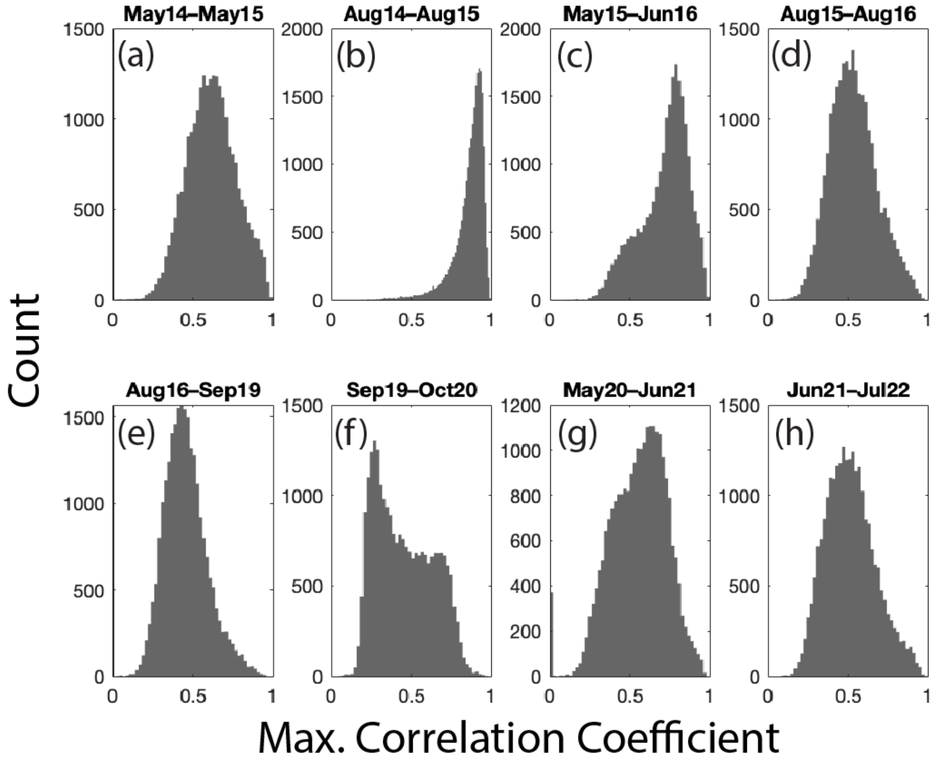

Figure 12. Histograms showing the distribution of the maximum correlation coefficients for each image pair at Sourdough with a time interval of one year or longer. Each panel (**a**–**h**) corresponds with results presented in the same panel labeled in Figure 6.

We tested these hypotheses with regard to the relationships between the number of outlying data points, the maximum correlation coefficient distribution, and the quality of change detection results by plotting the histograms for the August 2020/August 2022 image pair and the July 2021/August 2022 image pair at Galena Creek. Because the both the August 2020 and Augusut 2022 images were acquired using the UAS, the velocity field derived from this image pair has a low baseline uncertainty and a low amount of noisy regions in the velocity field. In comparison, the July 2021 image is a lower resolution and lower precision satellite product, leading to a higher baseline uncertainty and noise value for the July 2021/August 2022 velocity field. The distributions for Galena Creek (Figure 13) support our hypothesis that the velocity field quality can be characterized by both the size of the tail of outlying velocity magnitudes and the width of the distribution of the maximum correlation coefficients. In the case of the higher quality image pair at Galena Creek (August 2020/August 2022), the distributions contain a lower number of velocity magnitudes greater than 2 $\frac{\text{m}}{\text{yr}}$ and the peak of the maximum correlation coefficient distribution is narrower in comparison with the July 2021/August 2022 pair. Our observations of uncertainty patterns in the change detection results can be used to assess the propagation of error for future analyses using the velocity fields presented here. Evaluating the benefits and limitations of UAS, airborne, and satellite imaging platforms in regard to the measurement of rock glacier surface motion will contribute to the planning requirements of ongoing and future data acquisition campaigns [46,47].

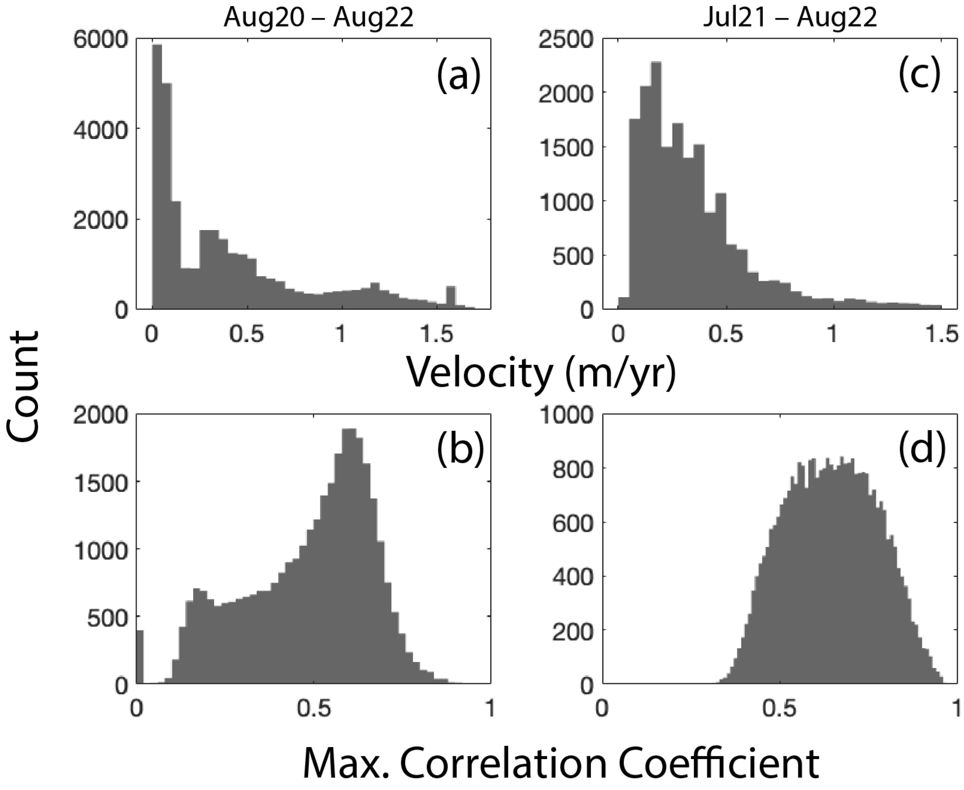

Figure 13. Histograms showing the distributions of velocity magnitude (**a**) and maximum correlation coefficient (**b**) for the August 2020/August 2022 image pair at Galena Creek and the velocity magnitude (**c**) and maximum correlation coefficient (**d**) for the July 2021/August 2022 hybrid image pair at Galena Creek.

4.2. Interpreted Flow History

The timescale required to transport a debris clast from the head of the glacier to the toe can estimated using the measured velocity fields, providing an estimate for the age of initial rock glacier accumulation. To obtain the age A_x at distance x from the rock glacier headwall, we integrate a smoothed profile of the inverse of calculated velocity magnitudes v_x (moving average window width = 5 pixels) along the central flowline for each rock glacier:

$$A_x = \int_0^x v_x^{-1}\,dx. \tag{1}$$

This method assumes a time-invariant velocity field along an interpreted flow path. The velocity field for Galena Creek has likely been dependent upon surface slope throughout its history, as it is today (Figure 14a); if the rock glacier was previously thicker and flowed faster due to higher driving stress, then our assumption of a constant velocity field would provide an upper bound for the age of the ice along the profile. Integrating the surface velocity profile of Galena Creek produces a terminus age of 3070 years (Figure 14a). This age falls between the estimated early neoglacial advance in Wyoming about 4000 years ago and the Audubon advance approximately 2000 to 1000 years ago [28]. Assuming that our age estimate is an upper bound, our results are most consistent with the rock glacier terminus of Galena Creek originating from the Audubon advance, while the debris-covered glacier comprising the upper two-thirds of the Galena Creek system contains ice that accumulated during the Little Ice Age (LIA), which spanned approximately the last half-millennium in the American Cordillera [48]. It is likely that this LIA advance interacted with the pre-existing rock glacier system, similarly to other landforms observed in the Swiss Alps and Chilean Andes [32–34]. This interaction of glacier ice and permafrost resulted in the complex topography and variable ice distribution found at the inflection in topography where they presently meet [31].

Our Galena Creek age profile is consistent with two calibrated radiocarbon measurements in leaf fragments at locations along the center flowline of Galena Creek (Figure 14a) [12]. The radiocarbon age acquired 100 m from the cirque headwall is 0–310 calendar years before present, and our velocity-derived age at this location is 180 years. Similarly, the radiocarbon age 800 m along the flow profile is 1410–1730 years before present, while the velocity-derived age is 1450 years. These independent measurements suggest that our method of age estimation is suitable for Galena Creek, where the low width/thickness ratio has allowed the velocity field to remain relatively consistent throughout the recent history of the rock glacier. Although Sulphur Creek is a close neighbor to Galena Creek, we did not perform a velocity profile analysis here, as the mid-glacier displacement vectors and elevation change since 1985 indicate substantial stagnation and surface subsidence in the past few decades, increasing the width/thickness ratio and likely invalidating the assumption of a time-invariant velocity field over the past few centuries.

We used the velocity profiles for three of the highest quality change detection results for Sourdough (August 2014/August 2015, August 2016/September 2019, and May 2014/July 2022) to better understand the propagation of uncertainty in the change detection results to the rock glacier age estimates (Figure 14b). The three profiles show rock glacier terminus ages ranging between 3,310 and 3,540 years. This range of ages is roughly consistent with the oldest of four late Holocene advances inferred from radiocarbon and tree ring dates [49], and although this indicates that these sites are older than the LIA, this result does not support the hypothesis that the ice in this population of rock glaciers in the Wrangell Mountains is related to the advance of the last glacial maximum (LGM), generally considered to be much more than 10,000 years ago.

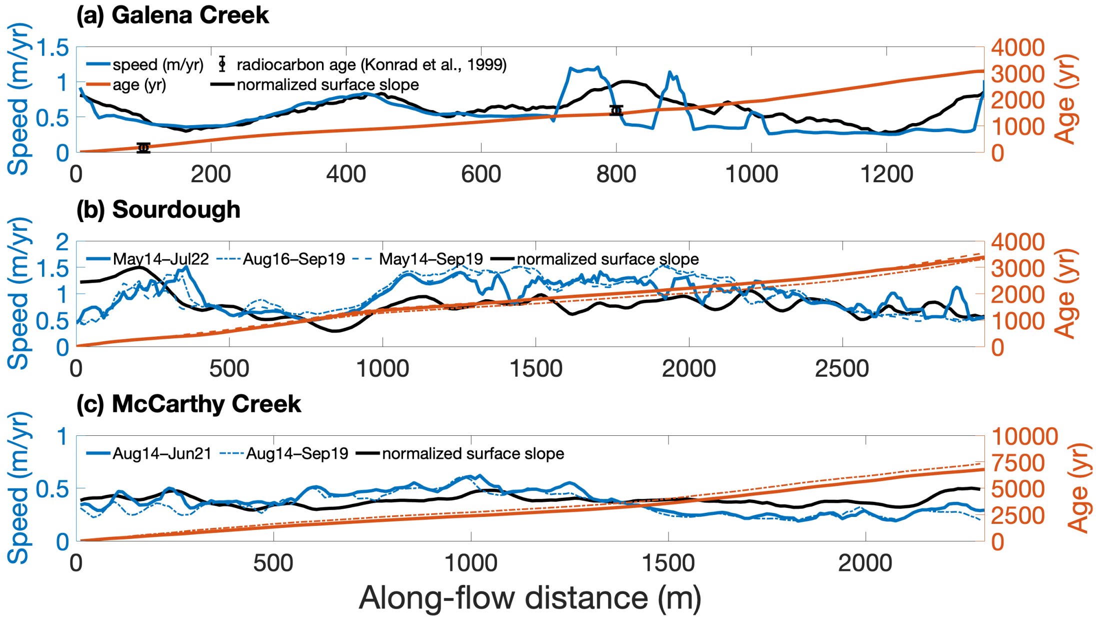

Figure 14. Velocity magnitudes (blue), age profiles (red), and normalized surface slopes (black) for (**a**) Galena Creek, including calibrated radiocarbon ages from [12] along the flow profile, (**b**) Sourdough, and (**c**) McCarthy Creek.

McCarthy Creek, just 2 km north of Sourdough, has a maximum velocity that is a factor of two less than that of Sourdough while covering a relatively similar length (Figure 14c). Using the August 2014/June 2021 velocity results for McCarthy Creek, which is the longest time interval without surface obfuscation due to snow, the estimated terminus age is approximately 6680 years. The August 2014/September 2019 image pair yields another high quality velocity field, and returns an age estimate of 7330 years. This range is about double the estimated age for Sourdough. Although this is an older age range, it is not consistent with an advance related to the LGM. While there is uncertainty in the exact path of a surface particle in comparison with our estimated flowline profiles, we do not expect this potential source of error to be the primary cause of the factor-of-two difference in the age calculations. Instead, this difference in estimated age for the two neighboring rock glaciers suggests the existence of local heterogeneities in rock glacier evolution, even if we assume that they are both related to the documented late Holocene ice advances in the Wrangell Mountains.

Heterogeneities in rock glacier evolution could influence variance in the surface velocity fields over time, refuting this age estimation's assumption of a time-invariant velocity field. Possible sources of differing velocity field evolution between the northward-flowing McCarthy Creek and southward-flowing Sourdough include the effect of slope aspect on accumulation and surface temperature as well as different series of rock glacier surges overriding less active older lobes. For example, if McCarthy Creek is in the process of stagnating while Sourdough's activity remains constant, our method would estimate an older age for McCarthy Creek due to the implication that slower surface velocities take longer to transport surface material along the length of the rock glacier. One possible line of evidence for a velocity field that has changed over time is the morphology and velocity distributions of the different lobes at Sourdough and McCarthy Creek. Sourdough consists of one major active lobe, where the peak velocity occurs within the steep trunk of the rock glacier, and one smaller active lobe to the east, where the velocity appears to be correlated to the surface slope as well. The western flank of Sourdough has two small steep lobes which are presently inactive (Figure 1a). These minor lobes are interpreted to be remnant overflow deposits from a past rock glacier advance when its thickness was greater than at present, indicating that this zone of maximum velocity has likely been correlated with the steep trunk of the rock glacier throughout its history. Even though the age estimate for Sourdough is taken to be an upper bound, we assume the relative velocities along its longitudinal profile have maintained similar trends in correlation with surface slope.

By contrast, McCarthy Creek consists of a large stagnant lobe to the north of the main active lobe, where the peak velocity is half that of Sourdough and which is found at the upper reaches of the rock glacier as opposed to the mid-glacier trunk, as it is at Sourdough. Sourdough is not substantially steeper than McCarthy Creek. In addition, McCarthy Creek displays no overflow lobes, suggesting that its movement may be more limited by its bedrock geometry and that the velocity field may be more susceptible to decreases in ice accumulation. Because the northern lobe of McCarthy Creek is presently stagnant and the peak velocity appears to have a lower correlation with surface slope (Figure 14c), it may be reasonable to assume that the northern lobe was previously more active and that the peak velocity would have been greater at the high slope regions on the rock glacier when the ice unit was thicker. All of these observations support the inference that McCarthy Creek has slowed over time, implying an overestimate of its total age; however, further work is needed to determine whether these differences in evolution between Sourdough and McCarthy Creek stem from heterogeneities in ice accumulation, debris input, valley geometry, the effects of slope aspect on insolation, or a combination of these processes.

In both Alaska and Wyoming, neighboring rock glaciers exhibit differences in flow rate distribution, suggesting that certain local controls may be influencing each rock glacier's evolution. As discussed above, the Alaskan rock glaciers differ significantly in their maximum flow speed, with Sourdough approaching 1.5 $\frac{\mathrm{m}}{\mathrm{yr}}$ and McCarthy Creek never exceeding 0.6 $\frac{\mathrm{m}}{\mathrm{yr}}$. Additionally, in Wyoming, Galena Creek's flow direction correlates with the down-valley topographical gradient and the flow velocity magnitude correlates with the magnitude of the longitudinal surface slope. Conversely, neighboring Sulphur Creek's velocity magnitude is greatest at the toe, and does not appear to be correlated with the longitudinal surface slope. The middle section of the glacier appears to be flowing perpendicular to the down-valley topography rather than parallel to it. This observation, combined with significant surface subsidence and a measured ice thicknesses of only about 10 m at this same location [31], reveals a recent rapid destabilization of the debris-covered ice in the upper Sulphur Creek basin. Although Galena Creek exhibits surface lowering as well, a comparison of its velocity-derived age with radiocarbon ages suggests no major deviations between its past and present velocity fields.

5. Conclusions

Our analysis demonstrates the capabilities and limitations of using multiple combinations of repeated imagery acquisition methods to perform photogrammetric change detection as a means of measuring rock glacier surface motion. The imagery acquired with the Phantom 4 RTK UAS had the highest success rate for detecting rock glacier surface flow due to this method's high image resolution and positioning accuracy. This effect is most apparent for the August 2020/August 2022 image pair at Galena Creek, Wyoming, where both images were acquired with the UAS. With this image pair, a strong flow signal was detected with a baseline measurement uncertainty of approximately 5 $\frac{\mathrm{cm}}{\mathrm{yr}}$. Airborne photogrammetry successfully detects rock glacier surface motion over annual time intervals, although the slightly diminished resolution and positioning accuracy due to the increased flight speed and altitude can propagate to the change detection results in comparison with the UAS-derived datasets. At each Alaska site (Sourdough and McCarthy Creek), strong flow signals were detected across the rock glacier surface with airborne imagery, especially for imaging intervals of three years or longer. The baseline uncertainty (20 $\frac{\mathrm{cm}}{\mathrm{yr}}$) is higher with the airborne method than that for image pairs where both images were acquired with the UAS.

While high-resolution satellite imagery provides the potential for consistent monitoring of rock glaciers, there is a tradeoff between this logistical convenience and the limitations of resolution and positioning for civilian data acquired from an orbital platform.

All of the orbital imagery used in this study required manual repositioning to improve co-registration with the images they were paired with, and the relatively coarse resolution limited the lower bound of the annual displacement magnitudes detectable by this method in comparison with the UAS and airborne platforms. The satellite imagery for both Wyoming field sites detected flow signals when paired with UAS and airborne data; however, the baseline uncertainty (40 cm) and the number of spurious displacement vectors caused by feature mismatches in the change detection were both the highest for all of the methods used.

A preliminary analysis of the rock glacier velocity fields shows that all of the study sites in Alaska and Wyoming likely originated during the early to middle Holocene, after the LGM and before the LIA. In addition to horizontal change detection, we used a combination of digital elevation models that are publicly available or generated with our photogrammetric processing method to estimate current thinning rates for each site. We found that both Wyoming sites exhibit a thinning signal that is consistent with the meteorological data and measured debris thickness, while neither of the the Alaska sites exhibits surface elevation change consistent with rock glacier thinning.

Due to the slow flow of rock glaciers in comparison with glaciers, all of the imagery applied to change detection experiments must have high-precision positioning information to reduce measurement error and detect a flow signal, especially when the time sampling interval is one year or less. This level of precision is vital for future studies focusing on remote sensing of seasonal patterns in rock glacier flow. With current technological resources, UAS imagery has the best resolution and positioning; however, it is limited to small spatial footprints at locations and times where the target is directly accessible. While airborne imagery provides a broader spatial extent and greater ease of data acquisition at regular time intervals for less accessible sites, it sacrifices resolution and precision. Satellite imagery offers a solution for regularly sampling a wide spatial area multiple times per year; however, the presently available data lack the resolution and precise positioning needed to achieve the lower uncertainty levels of UAS or airborne imagery. Increasing the number of high-resolution satellite imaging constellations for environmental studies would further improve the spatial and temporal capability to measure and monitor rock glaciers. We intend for the results of this study to be analyzed further using established glaciological principles, and our observations relating to the application of multi-platform change detection should be considered when planning campaigns to measure rock glacier surface motion.

Supplementary Materials: The following supporting information can be downloaded at: https://www.mdpi.com/article/10.3390/rs15194779/s1. Figure S1: Workflow diagram showing the methodology for combining UAS, airborne, and satellite data to measure each rock glacier's horizontal displacement and elevation change. Figure S2: Sourdough change detection using May 2014 base image. Figure S3: Galena Creek elevation change profile. Figure S4: Sourdough elevation profiles. Figure S5: McCarthy Creek elevation profiles. Figure S6: Surface boulder velocity measurements from 1997–2022 and comparison with remote change detection results.

Author Contributions: Conceptualization, all authors; methodology, all authors; software, T.M.M., R.A. and E.I.P.; validation, T.M.M. and R.A.; formal analysis, T.M.M., R.A. and E.I.P.; investigation, C.F.L., M.S.C., R.A., J.W.H., E.I.P. and T.M.M.; resources, J.W.H. and C.F.L.; data curation, C.F.L., M.S.C., R.A. and T.M.M.; writing—original draft preparation, T.M.M., R.A., E.I.P. and M.S.C.; writing—review and editing, all authors; visualization, T.M.M., E.I.P. and R.A.; supervision, J.W.H., J.S.L. and C.F.L.; project administration, J.W.H., J.S.L. and C.F.L.; funding acquisition, J.W.H., J.S.L. and C.F.L. All authors have read and agreed to the published version of the manuscript.

Funding: This research was funded by the NASA Solar System Workings program, grant number 80NSSC19K0561.

Data Availability Statement: The photogrammetry data, processed orthomosaics, DEMs, photogrammetric processing reports, horizontal change detection results, vertical elevation difference products, surface-based boulder position measurements, and the associated analysis code are openly available from the University of Arizona Research Data Repository (ReDATA) with the following DOI: https://doi.org/10.25422/azu.data.23272220.

Acknowledgments: We thank Kestrel Aerial Services for collecting the Wyoming airborne data presented here. This work utilized SkyMap50 satellite data made available through Soar. Extreme gratitude is felt for the field assistance provided by Brandon Tober, Stefano Nerozzi, Michael Daniel, and Rishi Chandra at the Wyoming sites and by Stefano Nerozzi, Tyler Kuehn, Victor Devaux-Chupin, and Bruno Belotti at Sourdough, Alaska. Many thanks to Noel Potter, Jr. and Noel Lewis Potter for sharing their boulder position data and for their valuable discussion regarding the history of exploration and glaciological research at the Wyoming field sites. Eric Yould provided essential logistical support throughout the years at the Alaska field sites. Thank you to three peer reviewers, whose comments and suggestions greatly improved this manuscript.

Conflicts of Interest: The authors declare no conflict of interest.

Abbreviations

The following abbreviations are used in this manuscript:

CIAS	Correlation Image Analysis Software
GNSS	Global Navigation Satellite System
GPR	Ground-Penetrating Radar
GDAL	Geospatial Data Abstraction Library
UAS	Uncrewed Aerial System
DEM	Digital Elevation Model
GCP	Ground Control Point
CP	Check Point
RMS	Root Mean Square
RTK	Real-Time Kinematic
LIA	Little Ice Age
LGM	Last Glacial Maximum
SNOTEL	Snowpack Telemetry

Appendix A. Thermal Conduction Model

To validate the remotely measured values of surface elevation change, we applied a simple melt model via 1D thermal conduction through the supraglacial debris layer. The objective of this model is to calibrate a realistic value for the thermal conductivity of the debris using the thinning rate measured with differenced DEMs at Galena Creek alongside temperature and snow depth data from the *Evening Star* meteorological station, which belongs to the SNOTEL network operated by the United States Department of Agriculture (station ID = 472). This station is located in the adjacent valley to the east of Galena Creek.

Using the SNOTEL data between the dates of 23 August 2020, and 8 August 2022, the melt rate was fixed to zero for dates with nonzero snow depth. For dates with zero snow, the melt rate ($\frac{\mathrm{m}}{\mathrm{day}}$) is provided by the following:

$$M = k\frac{dT}{dz}\frac{86{,}400}{\rho_{ice}L_f}, \tag{A1}$$

where k is the thermal conductivity of the debris layer, dT is simplistically assumed to be the SNOTEL air temperature measurement (T_{ice} = 0 °C), dz is the thickness of the debris layer, ρ_{ice} is the density of the ice (900 $\frac{\mathrm{kg}}{\mathrm{m}^3}$), and L_f is the latent heat of fusion (334,000 $\frac{\mathrm{J}}{\mathrm{kg}}$) [50]. For Galena Creek, we assume the debris thickness to be 1.5 m based on previous ice exposure observations and GPR measurements [1,3,31]. We test thermal conductivity values spanning the range of 0.3–1.8 $\frac{\mathrm{W}}{\mathrm{mK}}$, which is a feasible range for supraglacial debris, although it is likely that rock glacier debris resides on the lower end of this range due to its relatively high porosity [51,52]. The interpreted result of 20 cm cumulative melt during the

2020–2022 interval for Galena Creek is consistent with a thermal conductivity of 0.42 $\frac{\mathrm{W}}{\mathrm{mK}}$, approaching the lower bound of the plausible range (Figure A1b).

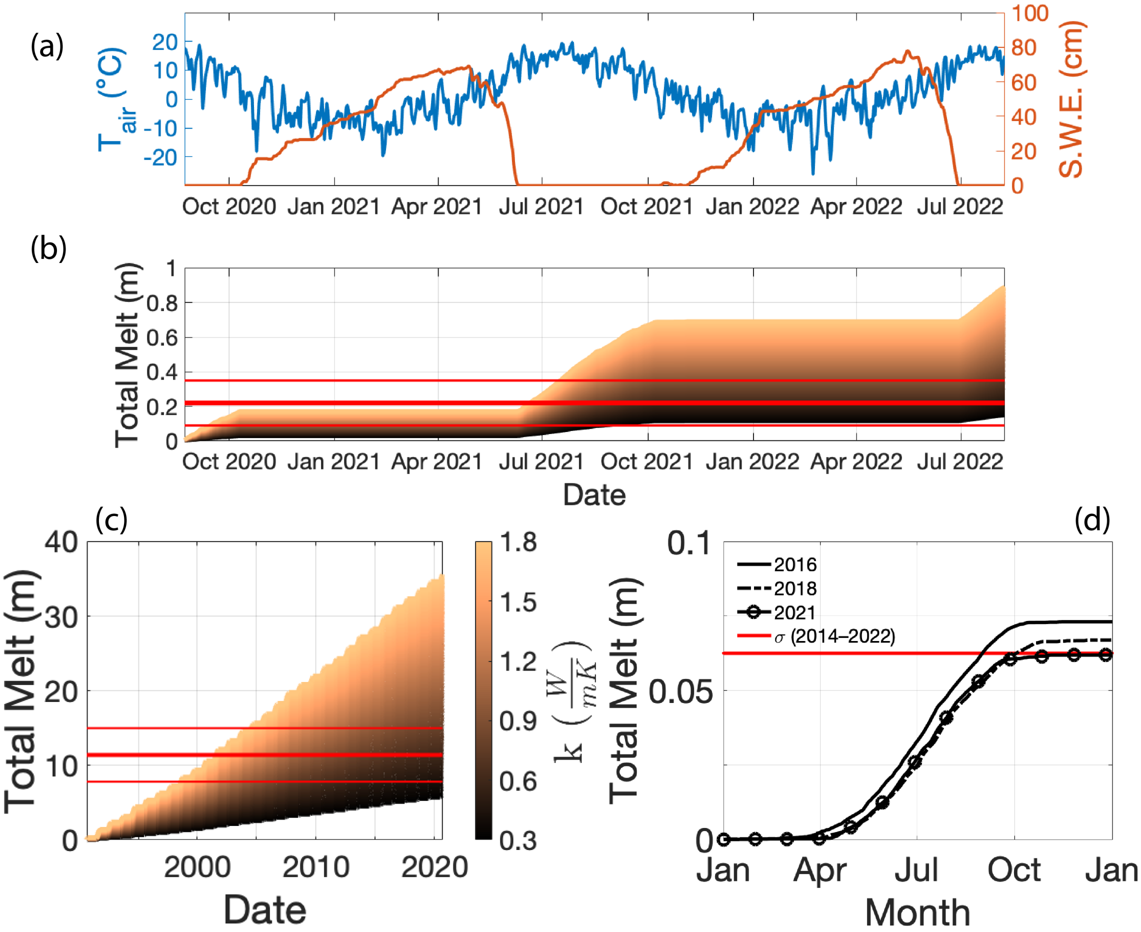

Figure A1. (**a**) Air temperature and snow water equivalent (SWE) data reported for the *Evening Star* SNOTEL site between 23 August 2020, and 8 August 2020. (**b**) Modeled melt over that same time interval for a range of possible thermal conductivity values for the debris layer and a debris thickness of 1.5 m. The horizontal red lines indicate the mean (thick line) and standard deviation (thin lines) of the photogrammetrically measured elevation change at upper Galena Creek. (**c**) Modeled melt using the *Evening Star* SNOTEL data between 1 September 1990, and 1 September 2020 for a debris thickness of 0.5 m as measured at upper Sulphur Creek in August 2020. The horizontal red lines indicate the expected mean (thick line) and standard deviation (thin lines) of the cumulative melt for that time period using melt rates measured between 1985 and 2020. (**d**) Modeled melt for Sourdough using air temperatures measured by an automated weather station near the rock glacier's toe, assuming a value of 3 m for the debris thickness and a thermal conductivity of 0.42 $\frac{\mathrm{W}}{\mathrm{mK}}$. The red line shows the standard deviation of the annual elevation change rate measured photogrammetrically between 2014 and 2022.

We applied the same thermal conduction model to the *Evening Star* SNOTEL data for the dates between 1 September 1990 and 1 September 2020 using a debris thickness of 0.5 m in order to test the remotely sensed cumulative surface lowering of between 18–28 m for upper Sulphur Creek over the 1985–2020 time interval. Although the SNOTEL data lack five years of data in comparison with the DEM interval, the thermal conduction results support the observation that upper Sulphur Creek thinned at a rate of tens of cm per year over three decades for plausible conductivities of the debris (Figure A1c), leading to cumulative melt well over 10 m for that period, further validating our photogrammetric results for Sulphur Creek.

We additionally tested the result of negligible surface elevation change for Sourdough and McCarthy Creek with the thermal conduction model using air temperature data acquired from an automated weather station on the lower lobe of Sourdough. Due to gaps in field campaigns, only the years 2016, 2018, and 2021 contained a complete and continuous calendar year of temperature data. We calculated the melt at Sourdough during each of these years using $dz = 3$ m and $k = 0.42\ \frac{\mathrm{W}}{\mathrm{mK}}$ (Figure A1d). Each of these years returns melt rates less than 10 $\frac{\mathrm{cm}}{\mathrm{yr}}$. Further, these melt rates are likely overestimates, as this weather station does not measure the presence of snow; thus, this conditional step is removed from the melt rate calculation. Removing the condition that the melt rate equals zero when the snow depth is greater than zero leads to an increase in the estimated melt rates for both Galena Creek and Sulphur Creek by a factor of approximately 1.3. After correcting the Sourdough melt rates for this factor, the resulting these rates are within about 1 $\frac{\mathrm{cm}}{\mathrm{yr}}$ of the standard deviation of the 2014–2022 elevation difference product.

Additionally, the location of the weather station at the toe of the rock glacier may bias this calculation towards higher melt rates, as its elevation at the bottom of the rock glacier implies that it has the highest temperature on the surface of the rock glacier assuming normal atmospheric lapse rates. In addition to the uncertainty in the temperature change with increasing elevation and the relationship of the air temperature to the debris surface temperature, this thermal conduction model is subject to uncertainties in the debris thickness. Although the meteorological data indicate that melt may be occurring at Sourdough and McCarthy Creek, the surface change due to this melt falls within the measurement uncertainty of the DEMs used to calculate the surface change over the 2014–2021 interval for McCarthy Creek and the 2014-2022 interval for Sourdough. Future refinement of rock glacier melt rate estimates should consider the effects of nonconductive heat fluxes [52].

References

1. Potter, N. Ice-Cored Rock Glacier, Galena Creek, Northern Absaroka Mountains, Wyoming. *Geol. Soc. Am. Bull.* **1972**, *83*, 3025–3057. [CrossRef]
2. Anderson, R.S.; Anderson, L.S.; Armstrong, W.H.; Rossi, M.W.; Crump, S.E. Glaciation of alpine valleys: The glacier–debris-covered glacier–rock glacier continuum. *Geomorphology* **2018**, *311*, 127–142. [CrossRef]
3. Petersen, E.I.; Levy, J.S.; Holt, J.W.; Stuurman, C.M. New insights into ice accumulation at Galena Creek Rock Glacier from radar imaging of its internal structure. *J. Glaciol.* **2019**, *66*, 1–10. [CrossRef]
4. Wahrhaftig, C.; Cox, A. Rock glaciers in the Alaska Range. *Geol. Soc. Am. Bull.* **1959**, *70*, 383–436. [CrossRef]
5. Haeberli, W.; Hallet, B.; Arenson, L.; Elconin, R.; Humlum, O.; Kääb, A.; Kaufmann, V.; Ladanyi, B.; Matsuoka, N.; Springman, S.; et al. Permafrost creep and rock glacier dynamics. *Permafr. Periglac. Process.* **2006**, *17*, 189–214. [CrossRef]
6. IPA Action Group; Rock Glacier Inventories and Kinematics (RGIK). Towards Standard Guidelines for Inventorying Rock Glaciers: Baseline Concepts (Version 4.2.2). Available online: www.rgik.org (accessed on 20 April 2023).
7. Kääb, A.; Vollmer, M. Surface Geometry, Thickness Changes and Flow Fields on Creeping Mountain Permafrost: Automatic Extraction by Digital Image Analysis. *Permafr. Periglac. Process.* **2000**, *11*, 315–326. [CrossRef]
8. Outcalt, S.I.; Benedict, J.B. Photo-Interpretation of two Types of Rock Glacier in the Colorado Front Range, U.S.A. *J. Glaciol.* **1965**, *5*, 849–856. [CrossRef]
9. White, S.E. Rock Glacier Studies in the Colorado Front Range, 1961 to 1968. *Arct. Alp. Res.* **1971**, *3*, 43–64. [CrossRef]
10. Francou, B.; Reynaud, L. 10 year surficial velocities on a rock glacier (Laurichard, French Alps). *Permafr. Periglac. Process.* **1992**, *3*, 209–213. [CrossRef]
11. Berthling, I.; Etzelmüller, B.; Eiken, T.; Sollid, J.L. Rock glaciers on Prins Karls Forland, Svalbard. I: Internal structure, flow velocity and morphology. *Permafr. Periglac. Process.* **1998**, *9*, 135–145. [CrossRef]
12. Konrad, S.K.; Humphrey, N.F.; Steig, E.J.; Clark, D.H.; Potter, N.; Pfeffer, W.T. Rock glacier dynamics and paleoclimatic implications. *Geology* **1999**, *27*, 1131–1134. [CrossRef]
13. Bucki, A.K.; Echelmeyer, K.A. The flow of Fireweed rock glacier, Alaska, U.S.A. *J. Glaciol.* **2004**, *50*, 76–86. [CrossRef]
14. Bertone, A.; Barboux, C.; Bodin, X.; Bolch, T.; Brardinoni, F.; Rafael Caduff, R.; Christiansen, H.H.; Darrow, M.M.; Delaloye, R.; Etzelmüller, B.; et al. Incorporating InSAR kinematics into rock glacier inventories: Insights from 11 regions worldwide. *Cryosphere* **2022**, *16*, 2769–2792. [CrossRef]
15. Brencher, G.; Handwerger, A.L.; Munroe, J.S. InSAR-based characterization of rock glacier movement in the Uinta Mountains, Utah, USA. *Cryosphere* **2021**, *15*, 4823–4844. [CrossRef]
16. Liu, L.; Millar, C.I.; Westfall, R.D.; Zebker, H.A. Surface motion of active rock glaciers in the Sierra Nevada, California, USA: Inventory and a case study using InSAR. *Cryosphere* **2013**, *7*, 1109–1119. [CrossRef]

17. Kääb, A. Remote Sensing of Mountain Glaciers and Permafrost Creep. *Schriftenreihe Physische Geographie Glaziologie und Geomorphodynamik*; Geographisches Institut der Universität Zürich: Zürich, Switzerland, 2005; Volume 48.
18. Robson, B.A.; MacDonell, S.; Ayala, Á.; Bolch, T.; Nielsen, P.R.; Vivero, S. Glacier and rock glacier changes since the 1950s in the La Laguna catchment, Chile. *Cryosphere* **2022**, *16*, 647–665. [CrossRef]
19. Gärtner-Roer, I.; Brunner, N.; Delaloye, R.; Haeberli, W.; Kääb, A.; Thee, R. Glacier–permafrost relations in a high-mountain environment: 5 decades of kinematic monitoring at the Gruben site, Swiss Alps. *Cryosphere* **2022**, *16*, 2083–2101. [CrossRef]
20. Vivero, S.; Bodin, X.; Farías-Barahona, D.; MacDonell, S.; Schaffer, N.; Robson, B.A.; Lambiel, C. Combination of Aerial, Satellite, and UAV Photogrammetry for Quantifying Rock Glacier Kinematics in the Dry Andes of Chile (30° S) Since the 1950s. *Front. Remote Sens.* **2021**, *2*, 784015. [CrossRef]
21. Lei, Y.; Gardner, A.; Agram, P. Autonomous Repeat Image Feature Tracking (autoRIFT) and Its Application for Tracking Ice Displacement. *Remote Sens.* **2021**, *13*, 749. [CrossRef]
22. Kenner, R.; Phillips, M.; Beutel, J.; Hiller, M.; Limpach, P.; Pointner, E.; Volken, M. Factors Controlling Velocity Variations at Short-Term, Seasonal and Multiyear Time Scales, Ritigraben Rock Glacier, Western Swiss Alps. *Permafr. Periglac. Process.* **2017**, *28*, 675–684. [CrossRef]
23. Heid, T.; Kääb, A. Repeat optical satellite images reveal widespread and long term decrease in land-terminating glacier speeds. *Cryosphere* **2012**, *6*, 467–478. [CrossRef]
24. Delaloye, R.; Lambiel, C.; Gärtner-Roer, I. Overview of rock glacier kinematics research in the Swiss Alps. *Geogr. Helv.* **2010**, *65*, 135–145. [CrossRef]
25. Jones, D.B.; Harrison, S.; Anderson, K.; Betts, R.A. Mountain rock glaciers contain globally significant water stores. *Sci. Rep.* **2018**, *8*, 2834. [CrossRef] [PubMed]
26. Barsch, D. The problem of the ice-cored rock glacier. In *Rock Glaciers*; Giardino, J.R., Shroder, J.E., Jr., Vitek, J.D., Eds.; Allen & Unwin: Boston, MA, USA, 1987; pp. 45–53.
27. Clark, D.H.; Steig, E.J.; Potter, N.; Gillespie, A.R. Genetic variability of rock glaciers. *Geogr. Ann. Ser. A Phys. Geogr.* **1998**, *80*, 175–182. [CrossRef]
28. Ackert, R.P., Jr. A Rock Glacier/Debris-Covered Glacier System at Galena Creek, Absaroka Mountains, Wyoming. *Geogr. Ann. Ser. A Phys. Geogr.* **1998**, *80*, 267–276. [CrossRef]
29. Potter, N.; Steig, E.J.; Clark, D.H.; Speece, M.A.; Clark, G.M.; Updike, A.B. Galena Creek rock glacier revisited—New observations on an old controversy. *Geogr. Ann. Ser. A Phys. Geogr.* **1998**, *80*, 251–265. [CrossRef]
30. Steig, E.J.; Fitzpatrick, J.J.; Potter, N.; Clark, D.H. The geochemical record in rock glaciers. *Geogr. Ann. Ser. A Phys. Geogr.* **1998**, *80*, 277–286. [CrossRef]
31. Meng, T.M.; Petersen, E.I.; Holt, J.W. Rock glacier composition and structure from radio wave speed analysis with dipping reflector correction. *J. Glaciol.* **2023**, *69*, 639–657. [CrossRef]
32. Kunz, J.; Kneisel, C. Glacier–permafrost interaction at a thrust moraine complex in the glacier forefield Muragl, Swiss Alps. *Geosciences* **2020**, *10*, 205. [CrossRef]
33. Bodin, X.; Rojas, F.; Brenning, A. Status and evolution of the cryosphere in the Andes of Santiago (Chile, 33.5° S.). *Geomorphology* **2010**, *118*, 453–464. [CrossRef]
34. Wee, J.; Delaloye, R. Post-glacial dynamics of an alpine Little Ice Age glacitectonized frozen landform (Aget, western Swiss Alps). *Permafr. Periglac. Process.* **2022**, *33*, 370–385. [CrossRef]
35. Potter, N. (Dickinson College, Carlisle, PA, USA). Personal communication, 2022.
36. Östrem, G. Ice Melting under a Thin Layer of Moraine, and the Existence of Ice Cores in Moraine Ridges. *Geogr. Ann.* **1959**, *41*, 228–230. [CrossRef]
37. Petersen, E.I.; Holt, J.W.; Levy, J.S.; Meng, T.M.; Tober, B.S.; Christoffersen, M.; Stuurman, C.M.; Cardenas, B. The transition from Alpine Glacier to Rock Glacier at Sulphur Creek, Wyoming. In Proceedings of the American Geophysical Union Fall Meeting, San Francisco, CA, USA, 9–13 December 2019; Abstract Number C41E–1506.
38. Potter, N.L.; Potter, N.; Retelle, M.J. Continued Movement and Ablation Monitoring, Galena Creek Rock Glacier, Absaroka Mountains, WY. In Proceedings of the Geological Society of America Annual Meeting, Denver, CO, USA, 25 September 2016; Abstract Number 81-14.
39. Nolan, M.; Larsen, C.; Sturm, M. Mapping snow depth from manned aircraft on landscape scales at centimeter resolution using structure-from-motion photogrammetry. *Cryosphere* **2015**, *9*, 1445–1463. [CrossRef]
40. Heid, T.; Kääb, A. Evaluation of existing image matching methods for deriving glacier surface displacements globally from optical satellite imagery. *Remote Sens. Environ.* **2012**, *118*, 339–355. [CrossRef]
41. U.S. Geological Survey. USGS 1/3 Arc Second n45w110: U.S. Geological Survey. 2023. Available online: www.sciencebase.gov/catalog/item/63c78c29d34e06fef14edbd2 (accessed on 13 February 2023).
42. Gesch, D.B.; Oimoen, M.J.; Evans, G.A. Accuracy assessment of the U.S. Geological Survey National Elevation Dataset, and comparison with other large-area elevation datasets—SRTM and ASTER. In *U.S. Geological Survey Open-File Report 2014–1008*; U.S. Geological Survey: Wriston, WV, USA, 2014
43. Debella-Gilo, M.; Kääb, A. Sub-pixel precision image matching for measuring surface displacements on mass movements using normalized cross-correlation. *Remote Sens. Environ.* **2011**, *115*, 130–142. [CrossRef]

44. Wirz, V.; Gruber, S.; Purves, R.S.; Beutel, J.; Gärtner-Roer, I.; Gubler, S.; Vieli, A. Short-term velocity variations at three rock glaciers and their relationship with meteorological conditions. *Earth Surf. Dyn.* **2016**, *4*, 103–123. [CrossRef]
45. Taylor, J.R. *An Introduction to Error Analysis: The Study of Uncertainties in Physical Measurements*, 2nd ed.; University Science Books: Sausalito, CA, USA, 1997.
46. Vivero, S.; Hendrickx, H.; Frankl, A.; Delaloye, R.; Lambiel, C. Kinematics and geomorphological changes of a destabilising rock glacier captured from close-range sensing techniques (Tsarmine rock glacier, Western Swiss Alps). *Front. Earth Sci.* **2022**, *10* , 1017949. [CrossRef]
47. Kaufmann, V.; Kellerer-Pirklbauer, A.; Seier, G. Conventional and UAV-Based Aerial Surveys for Long-Term Monitoring (1954–2020) of a Highly Active Rock Glacier in Austria. *Front. Remote Sens.* **2021**, *2*, 732744. [CrossRef]
48. Davis, P. Holocene glacier fluctuations in the American Cordillera. *Quat. Sci. Rev.* **1988**, *7*, 129–157. [CrossRef]
49. Wiles, G.C.; Jacoby, G.C.; Davi, N.K.; McAllister, R.P. Late Holocene glacier fluctuations in the Wrangell Mountains, Alaska. *Geol. Soc. Am. Bull.* **2002**, *114*, 896–908. [CrossRef]
50. Cuffey, K.M.; Paterson, W.S.B. *The Physics of Glaciers*, 4th ed.; Elsevier: New York, NY, USA, 2010.
51. Monnier, S.; Kinnard, C. Reconsidering the glacier to rock glacier transformation problem: New insights from the central Andes of Chile. *Geomorphology* **2015**, *238*, 47–55. [CrossRef]
52. Petersen, E.I.; Hock, R.; Fochesatto, G.J.; Anderson, L.S. The Significance of Convection in Supraglacial Debris Revealed Through Novel Analysis of Thermistor Profiles. *JGR Earth Surf.* **2022**, *127*, 47–55. [CrossRef]